

# Bayesian calibration with summary statistics for the prediction of xenon diffusion in $\text{UO}_2$ nuclear fuel

Pieterjan Robbe<sup>1</sup>, David Andersson<sup>2</sup>, Luc Bonnet<sup>1</sup>, Tiernan Casey<sup>1</sup>, Michael W. D. Cooper<sup>2</sup>, Christopher Matthews<sup>2</sup>, Khachik Sargsyan<sup>1</sup>, and Habib N. Najm<sup>1</sup>

<sup>1</sup>Sandia National Laboratories, Livermore, CA 94551, USA

<sup>2</sup>Los Alamos National Laboratory, Los Alamos, NM 37996, USA

February 22, 2023

## Abstract

The evolution and release of fission gas impacts the performance of  $\text{UO}_2$  nuclear fuel. We have created a Bayesian framework to calibrate a novel model for fission gas transport that predicts diffusion rates of uranium and xenon in  $\text{UO}_2$  under both thermal equilibrium and irradiation conditions. Data sets are taken from historical diffusion, gas release, and thermodynamic experiments. These data sets consist invariably of summary statistics, including a measurement value with an associated uncertainty. Our calibration strategy uses synthetic data sets in order to estimate the parameters in the model, such that the resulting model predictions agree with the reported summary statistics. In doing so, the reported uncertainties are effectively reflected in the inferred uncertain parameters. Furthermore, to keep our approach computationally tractable, we replace the fission gas evolution model by a polynomial surrogate model with a reduced number of parameters, which are identified using global sensitivity analysis. We discuss the efficacy of our calibration strategy, and investigate how the contribution of the different data sets, taken from multiple sources in the literature, can be weighted in the likelihood function constructed as part of our Bayesian calibration setup, in order to account for the different number of data points in each set of data summaries. Our results indicate a good match between the calibrated diffusivity and non-stoichiometry predictions and the given data summaries. We demonstrate a good agreement between the calibrated xenon diffusivity and the established fit from Turnbull et al. (1982), indicating that the dominant uranium vacancy diffusion mechanism in the model is able to capture the trends in the data.

## 1 Introduction

Uranium dioxide ( $\text{UO}_2$ ) is the fuel of choice in *light water reactors* (LWRs), the most common type of nuclear power plant in use [1]. Inside the reactor, uranium atoms fission into lighter elements, including noble gases such as xenon and krypton. The diffusion of these fission gas atoms, of which xenon atoms constitute the highest concentration, leads to significant performance concerns, as they cause a reduction of the fuel thermal conductivity, provoke fuel swelling, and contribute to a pressure buildup in the plenum, see, e.g., [2, 3]. It is therefore critical to better understand the behavior of these fission gases through modeling and simulation, especially in light of the recently developed new fuel types, such as Cr-doped  $\text{UO}_2$ , see, e.g., [4].

The diffusion of xenon in  $\text{UO}_2$  nuclear fuel has been studied extensively by both experiments [6, 7, 9, 10] and simulation [2, 3, 8, 11–17]. From these studies, it is understood that fission gas release is a multi-stage process, with the diffusion of individual gas atoms, assisted by the damage produced by fission fragments, as the essential material property that defines the fission gas response of a particular nuclear fuel.

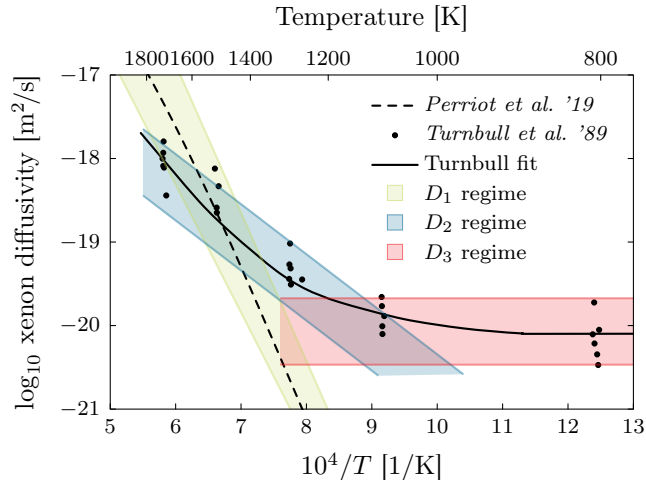


Figure 1: Experimental data and data fit for xenon diffusion in  $\text{UO}_2$ . The intrinsic diffusivity  $D_1$  is bounded by the fits from Davies & Long [5] and Matzke [6]. The intermediate and athermal regimes  $D_2$  and  $D_3$  are bounded by the re-evaluated data fit from Turnbull et al. [7]. Calculations from Perriot et al. [8] for the intrinsic diffusivity are also included.

Most existing fission gas release models rely on the analysis for the bulk xenon diffusivity performed in [9]. In this work, the fission gas diffusivity is divided into three different temperature ranges:  $D_1$  (temperatures larger than 1600 K),  $D_2$  (temperatures between 1600 K and 1200 K) and  $D_3$  (temperatures below 1200 K). These three regimes are shown in Figure 1.

In the high-temperature  $D_1$  or *intrinsic* regime, the diffusivity is dominated by the thermal defect concentrations. It is assumed that, in this regime, defects due to irradiation are quickly annealed and do not impact diffusion. In the intermediate-temperature  $D_2$  regime, radiation-induced defect concentrations start to dominate over the intrinsic mechanism. In the low-temperature  $D_3$  regime, the xenon diffusivity is driven directly by atomic mixing during radiation damage, exhibiting an athermal behavior.

Several modelling attempts have been made to explain the behavior of xenon diffusion in  $\text{UO}_2$ , see, e.g., [8, 17–19]. Despite the progress made in these recent works, the precise mechanisms underlying the diffusion process are still being investigated. For example, the cluster dynamics simulations from [19] for the prediction of the xenon diffusivity under irradiation in the  $D_2$  regime underpin a mechanistic diffusion model that describes the complex interactions between point defects in the  $\text{UO}_2$  lattice and individual xenon atoms. This model contains a total of 183 parameters, including reaction energies, binding energies, activation energies and attempt frequencies for all lattice defects. While a first-principles approach was used to develop this model, a significant uncertainty is associated with all of these parameters.

The cluster dynamics simulations in [19] were performed using *Centipede*. *Centipede* predicts the uranium diffusivity  $D_{\text{U}}^{\text{theq}}$  and xenon diffusivity  $D_{\text{Xe}}^{\text{theq}}$  under thermal equilibrium conditions, as well as the uranium diffusivity  $D_{\text{U}}^{\text{irr}}$  and xenon diffusivity  $D_{\text{Xe}}^{\text{irr}}$  under irradiation, as a function of temperature, oxygen partial pressure, and fission rate. In order to predict the diffusion coefficients, *Centipede* also models the fuel non-stoichiometry (i.e., the deviation  $x$  of  $\text{UO}_{2\pm x}$  from perfect stoichiometric  $\text{UO}_2$ ). Figure 2 contains an illustration of the diffusivity predictions, and Figure 3 contains an illustration of the non-stoichiometry predictions. Note that the diffusivity predictions are plotted as a function of temperature  $T$ , while the non-stoichiometry predictions are shown as a function of both  $T$  and oxygen partial pressure ( $p_{\text{O}_2}$ ).

In our calibration setup, the *Centipede* outputs will be matched with the experimental data summaries taken from previous diffusion, gas release and thermodynamic experiments reported in the literature, in particular [5, 7, 9, 20–28]. These data sets are invariably reported as summary

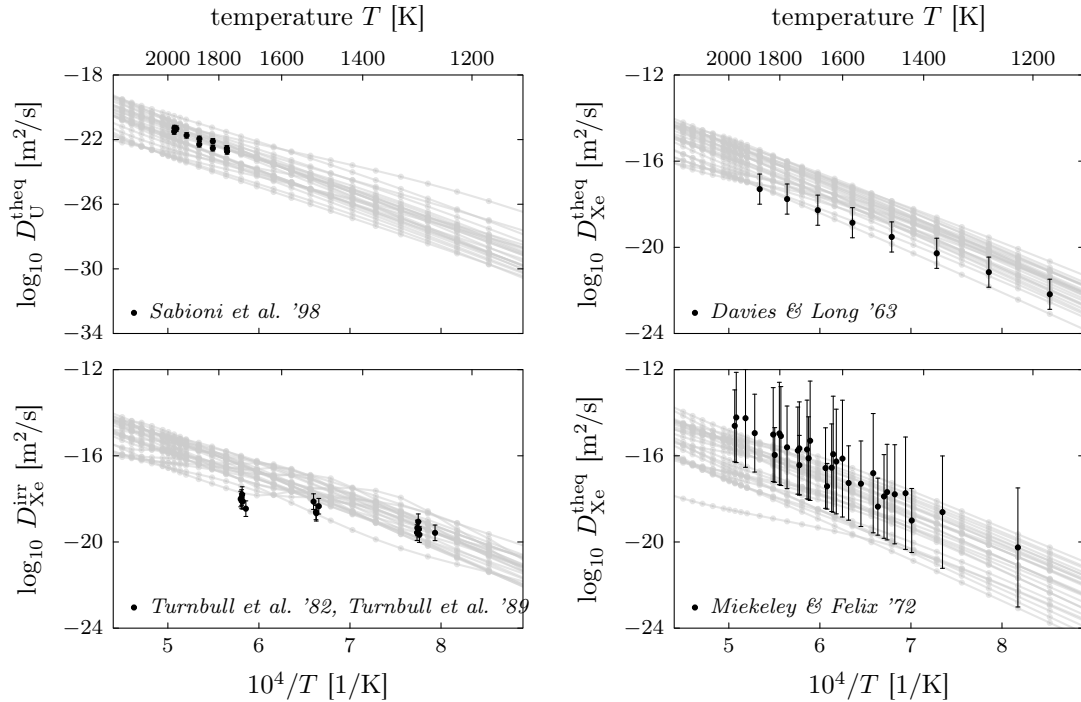


Figure 2: Measurement values and associated errors for each set of experimental data summaries. Also shown are a set of 25 **Centipede** predictions of the diffusivity quantity predicted by each experiment at 26 different temperatures, with input parameter values drawn from a uniform distribution between the corresponding lower and upper bounds of each, and under the operating conditions corresponding to each set of experimental data summaries, see [Table 1](#).

statistics, i.e., each data point contains a mean measurement value with an associated error. Again, we refer to [Figure 2](#) for an illustration. An overview of the different data sets is shown in [Table 1](#).

A Bayesian calibration methodology for this setting, in which only summary statistics are available, is the *data-free inference* (DFI) approach. DFI has been introduced in [29], and was applied in various settings in, amongst others, [30–33]. In a context where data summaries are available, but the original data is not, DFI generates synthetic data on the experimentally observed outputs, that is consistent with the reported summary statistics when used to estimate model parameters using Bayesian inference. The procedure entails a nested inference scheme that evolves in both the data and parameter spaces. The computational complexity of the DFI procedure, and the need to build physically meaningful data-generating models for each experiment, renders its full utilization challenging in the present multi-experiment setting. We introduce a modification of the DFI method discussed in [31], that simplifies the synthetic data-generation process, and is computationally tractable.

Our approach considers the entire ensemble of data summaries across all experiments to learn the joint distribution of all uncertain parameters in the model. Since there may be a different number of data points in each set of data summaries, the calibration result may be dominated by data sets that contain a large number of measurements, such as the Miekeley & Felix or stoichiometric data set, see [Table 1](#). In order to avoid this, we propose a weighted approach where the contribution of each data set to the likelihood is normalized by the number of data points it contains.

To further reduce the computational burden, we replace the actual **Centipede** evaluations by a computationally inexpensive surrogate model. In particular, we choose to fit a polynomial chaos expansion (PCE) surrogate model to the **Centipede** outputs, see [34, 35].

The remainder of this paper is organized as follows. First, in [Section 2](#), we provide more details on the cluster dynamics simulation code **Centipede**. Next, in [Section 3](#), we outline our parameter

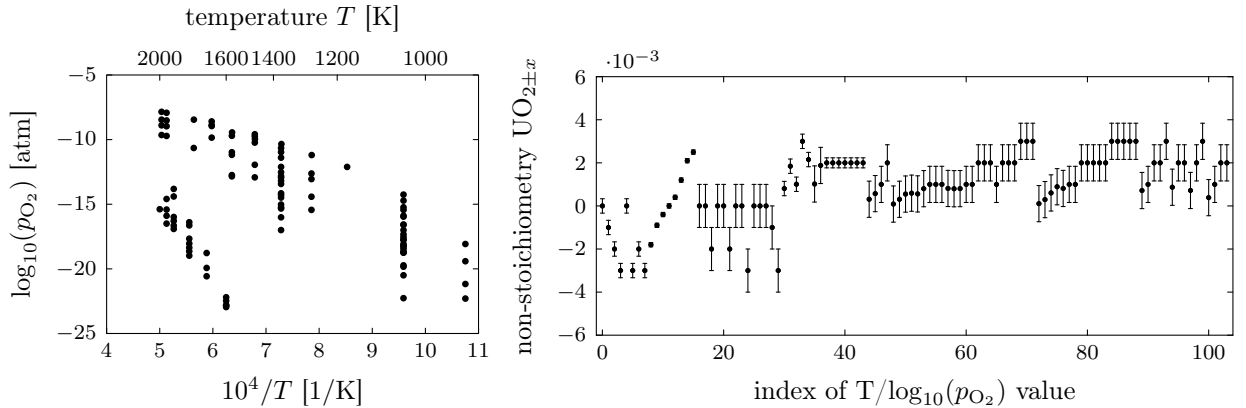


Figure 3: Measurement values and associated errors for the stoichiometric data from [20–27]. The figure on the left illustrates how the index of  $T/\log_{10}(p_{O_2})$  is mapped to a  $(T, \log_{10}(p_{O_2}))$  pair, see Table 8.

$d$	experimental data summaries	reference(s)	measured quantity	$N_d$	Hf_pO2 [eV]	T0 [K]
1	Sabioni et al.	[28]	$D_U^{\text{theq}}$	10	5.10	1973
2	Davies & Long	[5]	$D_{Xe}^{\text{theq}}$	8	5.10	1973
3	Turnbull et al.	[7, 9]	$D_{Xe}^{\text{irr}}$	16	5.10	1973
4	Miekeley & Felix	[36]	$D_{Xe}^{\text{theq}}$	32	6.11	1973
5	stoichiometry	[20–27]	$UO_{2\pm x}$	104	-	-

Table 1: Overview of the  $D = 5$  different data sets in the calibration setup. The operating conditions Hf\_pO2 and T0 vary between the different experiments, and will be estimated in the present study. The listed values are current best estimates.

estimation strategy. More details on the surrogate construction are provided in Section 4. In Section 5, we report the results obtained by applying our calibration framework to characterize the uncertainty in the atomistic-scale model parameters of Centipede, and provide an interpretation of these results. Finally, a conclusion and pointers to future work are given in Section 6.

## 2 Simulation of fission gas diffusivity in $UO_2$

To compute the diffusivities under thermal equilibrium in the  $D_1$  regime, an analytical point defect model, based on density functional theory (DFT) calculations for the energies and (semi-)empirical potential (EP) calculations for the entropies, was proposed in [8]. It was shown that, in this regime, the active diffusion mechanism is a vacancy mechanism, i.e., a single xenon atom occupying a cluster consisting of two uranium vacancies and one oxygen vacancy. The predicted xenon diffusivities depend on the non-stoichiometry of the fuel ( $UO_{2\pm x}$ ), which, in turn, is governed by the prescribed  $p_{O_2}$ . The resulting xenon diffusivity agrees reasonably well with the experimental data summaries due to Davies & Long, see [5], which is considered to be the most accurate data for application in fuel performance codes in this high-temperature regime, see [7, 9].

The athermal diffusivity in the low-temperature  $D_3$  regime has been estimated from molecular dynamics (MD) simulations for the atomic mixing induced by electronic stopping of fission fragments causing thermal spikes in [17].

A model for the evolution of point defects and xenon clusters under irradiation in  $UO_2$  in the  $D_2$  regime has been introduced in [19], as the analytical point defect model that is valid under the thermal equilibrium conditions in the  $D_1$  regime cannot be used under irradiation. The model is based on the free-energy cluster dynamics framework from [18]. To capture the non-equilibrium response due to irradiation, the creation of point defects due to irradiation, as well as the interaction

of point defects or clusters of point defects with other defects (including their self-interactions) and the interaction with lattice sinks, must be modelled. **Centipede**, the cluster dynamics simulator that implements the model from [18], solves a set of coupled ordinary differential equations (ODEs) that determine the atom fraction or concentration  $X_\delta$  of a defect  $\delta$  at a given temperature  $T$ . The atom fraction  $X_\delta$  of a defect  $\delta$  satisfies

$$\frac{dX_\delta}{dt} = \underbrace{\dot{B}_\delta}_{\text{defect production}} + \underbrace{\sum_\gamma \dot{R}_{\delta,\gamma}(X_\delta, X_\gamma, T, G)}_{\text{interactions with other defects } \gamma} - \underbrace{\sum_\sigma \dot{S}_{\delta,\sigma}(X_\delta, X_\sigma, T, G)}_{\text{interactions with sinks } \sigma}, \quad (1)$$

where  $\dot{R}_{\delta,\gamma}$  is the reaction rate,  $\dot{S}_{\delta,\sigma}$  is the sink rate, and  $G$  is the free energy in the system, see [19, equation (1)]. The free energy governs the direction of the reaction and provides a natural way to account for non-stoichiometry and other thermodynamic considerations. **Centipede** solves the coupled set of reaction equations in (1) for the condition where  $dX_\delta/dt = 0$  for all  $\delta$ , i.e., the pseudo-steady state condition, which provides the concentration of all point defects, clusters of point defects, and xenon clusters. Note that each defect species is dependent on all other point defects, resulting in a system of coupled ODEs that rapidly grows as the number of different species used to describe the system is increased. It should also be noted that, without the presence of irradiation, the solution to (1) reduces to the solution of the analytical model that is used to describe the thermal equilibrium case. The sought-after diffusivities may be calculated by considering the concentration and mobility of each individual cluster, see [19, equation (4)].

The reaction rates  $\dot{R}_{\delta,\gamma}$  depend on the change in the chemical potential (or *driving force*). This driving force can be formulated as a change in the free energy  $G$ . In order to calculate the necessary reaction rates, an extensive set of atomistic input parameters is required. This includes thermodynamic (binding energies DFT [eV] and entropies  $S$  [ $k_B$ ]) and kinetic (activation energies  $Q$  [eV] and attempt frequencies  $w$  [THz]) properties of xenon-vacancy clusters and interstitial defects. Lower and upper bounds for these parameters were determined based on the results reported in [8, 19], and have been collected in Table 9.

Additionally, there are uncertainties in the DFT binding energies originating from corrections applied to the values obtained from DFT calculations of charged supercells, see [8]. In particular, two correction terms are added to each binding energy, that scale quadratically with the charge of the defect. These correction terms depend on the parameters `charge_correction_DFT` and `charge_sq_correction_DFT`, respectively, see Table 9. The correction terms allow us to capture the systematic error in the binding energies.

Note that the formation energies of point defects are dependent on the  $p_{O_2}$  of the system. In [18], a simple model was proposed for the temperature-dependent  $p_{O_2}$ , that depends on two experimentally defined parameters: the enthalpy for the reaction controlling the oxygen potential (`Hf_pO2`) and the temperature at which  $UO_2$  is assumed stoichiometric (`T0`) for the particular value of `Hf_pO2`, see [18, equation (34)]. Both `Hf_pO2` and `T0` change the degree of non-stoichiometry  $UO_{2\pm x}$ , the former through the enthalpy and the latter via the entropy. When combined with the point defect formation energies, `Hf_pO2` and `T0` describe an Arrhenius relation for  $p_{O_2}$  as function of temperature. This relation is controlled by the active oxygen buffering reaction in each experiment and, by extension, the details of the experimental setup, which are rarely reported. In our numerical results in Section 5, we will incorporate these two data-set-dependent parameters, and they are to be estimated along with the other parameters in the model.

Finally, we mention that **Centipede** focuses on accurately capturing the intrinsic diffusivity of fission gas in the chemistry and irradiation response of point defects and relatively small defect clusters with up to about 10 uranium and 20 oxygen vacancies interacting with a single xenon atom. Any cluster larger than roughly 10 uranium vacancies, or containing more than one xenon atom,

acts as an immobile sink, rather than as a mobile cluster, and consequently does not contribute to diffusion. This distinguishes it from the `XoLot1` cluster dynamics code from [37], which simulates clusters of xenon atoms containing up to millions of atoms, needed to describe the full intra-granular behavior of fission gas. The coupling of `Centipede` and `XoLot1` to describe the full xenon-vacancy phase space in a single simulation is currently ongoing.

### 3 Bayesian calibration for summary statistics

In this section, we outline our Bayesian calibration strategy. Our goal is to perform Bayesian inference, that is, given the experimental data summaries  $\mathcal{D}$  and a prior  $p(\boldsymbol{\nu})$  on the `Centipede` model parameters  $\boldsymbol{\nu} \in \mathbb{R}^s$ , with  $s$  the number of parameters, we want to compute the posterior distribution  $p(\boldsymbol{\nu}|\mathcal{D})$ , i.e., the probability density on the parameters  $\boldsymbol{\nu}$  given that we observe the experimental data summaries  $\mathcal{D}$ . According to Bayes' rule, the prior and posterior are related through the likelihood function  $\mathcal{L}_{\mathcal{D}}(\boldsymbol{\nu})$  as

$$p(\boldsymbol{\nu}|\mathcal{D}) \propto \mathcal{L}_{\mathcal{D}}(\boldsymbol{\nu})p(\boldsymbol{\nu}), \quad (2)$$

where  $\mathcal{L}(\boldsymbol{\nu}) := p(\mathcal{D}|\boldsymbol{\nu})$  expresses the likelihood of observing the data given the parameter values  $\boldsymbol{\nu}$ . In [Section 3.1](#), we will briefly discuss the different components of [equation \(2\)](#) in more detail, before outlining our calibration strategy in [Section 3.2](#), and formulating an expression for the likelihood in [Section 3.3](#).

#### 3.1 Bayesian calibration

We start by formalizing the available information shown in [Figures 2 and 3](#). The data summaries  $\mathcal{D}$  are composed of  $D = 5$  sets of experimental data summaries  $\mathcal{D}_d$ ,  $d = 1, 2, \dots, D$ , with  $N_d$  measurement stations  $\boldsymbol{x}_d^{(n)}$ ,  $n = 1, 2, \dots, N_d$ , in each set. These measurement stations  $\boldsymbol{x}_d^{(n)}$  correspond to different temperatures  $T$  and/or  $p_{\text{O}_2}$  values. An overview of these data summaries is shown in [Table 1](#). Each set  $\mathcal{D}_d$  consists of mean values  $y_d^{(n)}$  with associated uncertainties  $s_d^{(n)}$ , defined at the  $N_d$  measurement stations  $\boldsymbol{x}_d^{(n)}$ ,  $n = 1, 2, \dots, N_d$ , i.e.,

$$\mathcal{D}_d = \{\boldsymbol{x}_d^{(n)}, y_d^{(n)}, s_d^{(n)}\}_{n=1}^{N_d}, \quad d = 1, 2, \dots, D \quad (3)$$

and  $\mathcal{D} = \{\mathcal{D}_d\}_{d=1}^D$ .

Let  $f_d^{\text{true}}(\boldsymbol{x})$  be the true model that provides the exact values of the quantity being measured in  $\mathcal{D}_d$ . The true values  $f_d^{\text{true}}(\boldsymbol{x}_d^{(n)})$  are not directly accessible, as observations are corrupted by noise. For example, in the case of additive Gaussian noise, one may assume that the measured data  $q_d^{(n)}$  are available as

$$q_d^{(n)} := f_d^{\text{true}}(\boldsymbol{x}_d^{(n)}) + \sigma_d^{(n)}\eta_d^{(n)},$$

where  $\sigma_d^{(n)}$ ,  $n = 1, 2, \dots, N_d$ , is the standard deviation of the noise of the measurement at station  $\boldsymbol{x}_d^{(n)}$ , and where the  $\eta_d^{(n)}$  are drawn from a standard normal distribution, i.e.,  $\eta_d^{(n)} \sim \mathcal{N}(0, 1)$ . Given the noisy observations  $q_d^{(n)}$  of  $f_d^{\text{true}}(\boldsymbol{x}_d^{(n)})$ , we may use this information, along with a prior distribution  $p(\boldsymbol{\nu})$ , to estimate the parameters  $\boldsymbol{\nu}$  in an *assumed model*  $f_d(\boldsymbol{x}, \boldsymbol{\nu})$ . In our setting, this model  $f_d(\boldsymbol{x}, \boldsymbol{\nu})$  will be the `Centipede` predictions of the quantity being measured in the  $d$ th data set.

In particular, suppose we are given a set of observations  $\mathcal{Q}_d := \{q_d^{(n)}\}_{n=1}^{N_d}$  at  $\boldsymbol{x}_d^{(n)}$ ,  $n = 1, 2, \dots, N_d$ . If we assume that the observation errors  $\sigma_d^{(n)}\eta_d^{(n)}$  are independent, then the likelihood takes the form

$$\begin{aligned} \mathcal{L}_{\mathcal{Q}_d}(\boldsymbol{\nu}) &:= p(\mathcal{Q}_d|\boldsymbol{\nu}) \\ &= \prod_{n=1}^{N_d} \frac{1}{\sigma_d^{(n)}\sqrt{2\pi}} \exp\left(-\frac{\left(q_d^{(n)} - f_d(\boldsymbol{x}_d^{(n)}, \boldsymbol{\nu})\right)^2}{2\sigma_d^{(n)2}}\right). \end{aligned}$$

Equivalently, the log-likelihood becomes

$$\log \mathcal{L}_{\mathcal{Q}_d}(\boldsymbol{\nu}) = -\frac{1}{2} \sum_{n=1}^{N_d} \left[ \log(2\pi\sigma_d^{(n)2}) + \frac{\left(q_d^{(n)} - f_d(\mathbf{x}_d^{(n)}, \boldsymbol{\nu})\right)^2}{\sigma_d^{(n)2}} \right].$$

A full log-likelihood for the calibration problem that involves observations  $\mathcal{Q} := \{\mathcal{Q}_d\}_{d=1}^D$  from  $D$  independent experiments can simply be constructed as

$$\log \mathcal{L}_{\mathcal{Q}}(\boldsymbol{\nu}) = \sum_{d=1}^D \log \mathcal{L}_{\mathcal{Q}_d}(\boldsymbol{\nu}),$$

and samples of the posterior  $p(\boldsymbol{\nu}|\mathcal{Q})$  can then be obtained by Markov chain Monte Carlo (MCMC), see, e.g., [38] and Section B.

In our current setup, however, the observations  $\mathcal{Q}$  are generally not available. Instead, we are given *summary statistics*, such as a mean or a standard deviation of processed observations, as indicated in equation (3). A DFI framework where data summaries involving measurement values and associated error bars on model outputs are available has been proposed in [31]. In this work, two interpretations of error bars were discussed. In a first interpretation, the error bars are considered as quantifying the degree of error or scatter in the measurements, while, in the second interpretation, they are considered as quantifying the resulting uncertainty in the measured quantity. Here, we interpret the error bars as the latter type, which we believe to be a more natural interpretation of the reported measurements.

The DFI method provides a joint posterior density on both the data and model parameters by enforcing consistency between the reported summary statistics and the statistics of the data [39,40]. The algorithm entails a nested sampling procedure, with an outer MCMC chain on the data space, and an inner MCMC chain on the parameter space. At each step of the outer chain, a new data set is proposed, after which the inner chain is executed in full to provide samples of the associated posterior, which are then used to check for consistency of the proposed data set with the reported summary statistics. Each accepted data set provides a consistent posterior on the model parameters. The final *pooled posterior* is ultimately obtained by combining the posteriors for all consistent data sets.

We propose a simplified DFI construction that avoids the nested MCMC chain construction of the original scheme, thus increasing the computational efficiency. We presume a Gaussian distribution for the synthetic data on the quantity of interest at each measurement station. For each data set, these distributions are scaled such that statistics derived from the model predictions approximate the reported error bars. We then define a consistent data set as one for which the statistics computed from the data are, up to a tolerance, equal to the reported summary statistics. We illustrate below that this consistency metric, along with the presumed Gaussian distribution for the synthetic data, replaces the outer inference problem in DFI by an optimization procedure, which is more computationally tractable. The use of this presumed distribution distinguishes our approach from [31].

### 3.2 Bayesian calibration with summary statistics

We start by defining a collection of  $K_d$  synthetic data sets  $\mathcal{Z}_d^{(k)} := \{z_d^{(n,k)}\}_{n=1}^{N_d}$ ,  $k = 1, 2, \dots, K_d$ , where

$$z_d^{(n,k)} \sim \mathcal{N}\left(y_d^{(n)}, \beta_d s_d^{(n)2}\right), \quad (4)$$

with  $y_d^{(n)}$  and  $s_d^{(n)}$  the measurement value and error respectively, see (3), and where  $\beta_d > 0$  is a scale factor for the variance. Hence, the data set  $\mathcal{Z}_d^{(k)}$  contains synthetic observations that are sampled

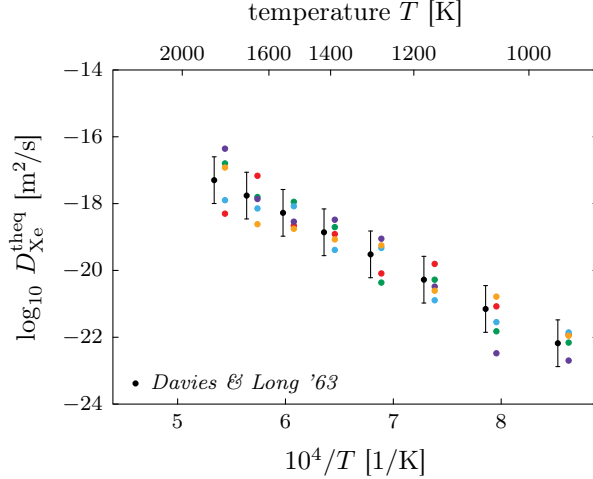


Figure 4: Example of synthetic data sets for the Davies & Long experimental data summaries using  $K_d = 5$  and  $\beta_d = 1$ . Different colors indicate different values for  $k$ ,  $1 \leq k \leq K_d$ .

from a Gaussian distribution centered at  $y_d^{(n)}$  for each  $n = 1, 2, \dots, N_d$ , and with a variance that can be tuned by choosing appropriate values for  $\beta_d$ . An example of a collection of synthetic data sets  $\mathcal{Z}_d^{(k)}$  for the Davies & Long experimental data summaries with  $K_d = 5$  and  $\beta_d = 1$  is shown in Figure 4.

Each synthetic data set  $\mathcal{Z}_d^{(k)}$ ,  $k = 1, 2, \dots, K_d$ , represents an opinion about the true posterior through its corresponding log-likelihood

$$\log \mathcal{L}_{\mathcal{Z}_d^{(k)}}(\boldsymbol{\nu}) := -\frac{1}{2} \sum_{n=1}^{N_d} \left[ \log(2\pi\beta_d s_d^{(n)2}) + \frac{(z_d^{(n,k)} - f_d(\mathbf{x}_d^{(n)}, \boldsymbol{\nu}))^2}{\beta_d s_d^{(n)2}} \right].$$

These  $K_d$  different opinions can be combined using *logarithmic pooling*, see [29]. This can be accomplished by gathering all synthetic data sets  $\mathcal{Z}_d^{(k)}$  into a single data set  $\mathcal{Z}_d := \{\mathcal{Z}_d^{(k)}\}_{k=1}^{K_d}$ , and setting up an inference problem that uses an averaged log-likelihood

$$\begin{aligned} \log \mathcal{L}_{\mathcal{Z}_d}(\boldsymbol{\nu}) &:= \frac{1}{K_d} \sum_{k=1}^{K_d} \log \mathcal{L}_{\mathcal{Z}_d^{(k)}}(\boldsymbol{\nu}) \\ &= -\frac{1}{2} \sum_{n=1}^{N_d} \left[ \log(2\pi\beta_d s_d^{(n)2}) + \frac{1}{K_d \beta_d s_d^{(n)2}} \sum_{k=1}^{K_d} (z_d^{(n,k)} - f_d(\mathbf{x}_d^{(n)}, \boldsymbol{\nu}))^2 \right]. \end{aligned}$$

Logarithmic average pooling has a number of desirable properties over simple linear pooling. The latter uses an arithmetic averaging of the posteriors  $p(\boldsymbol{\nu}|\mathcal{Z}_d^{(k)})$ . We refer to [41] for more details.

Once we obtain the posterior density  $p(\boldsymbol{\nu}|\mathcal{Z}_d)$  on the model parameters, samples from the posterior can be propagated through the assumed forward model  $f_d(\mathbf{x}, \boldsymbol{\nu})$ , in order to obtain samples from the *pushforward posterior* density  $p(f_d(\mathbf{x}, \boldsymbol{\nu})|\mathcal{Z}_d)$ . The pushforward posterior is the target of the forward uncertainty quantification process given the parameter posterior  $p(\boldsymbol{\nu}|\mathcal{Z}_d)$ .

From  $p(f_d(\mathbf{x}, \boldsymbol{\nu})|\mathcal{Z}_d)$ , we can estimate statistics on model outputs which can be compared to the reported summary statistics  $s_d^{(n)}$  to decide whether the proposed data set  $\mathcal{Z}_d$  is consistent. In

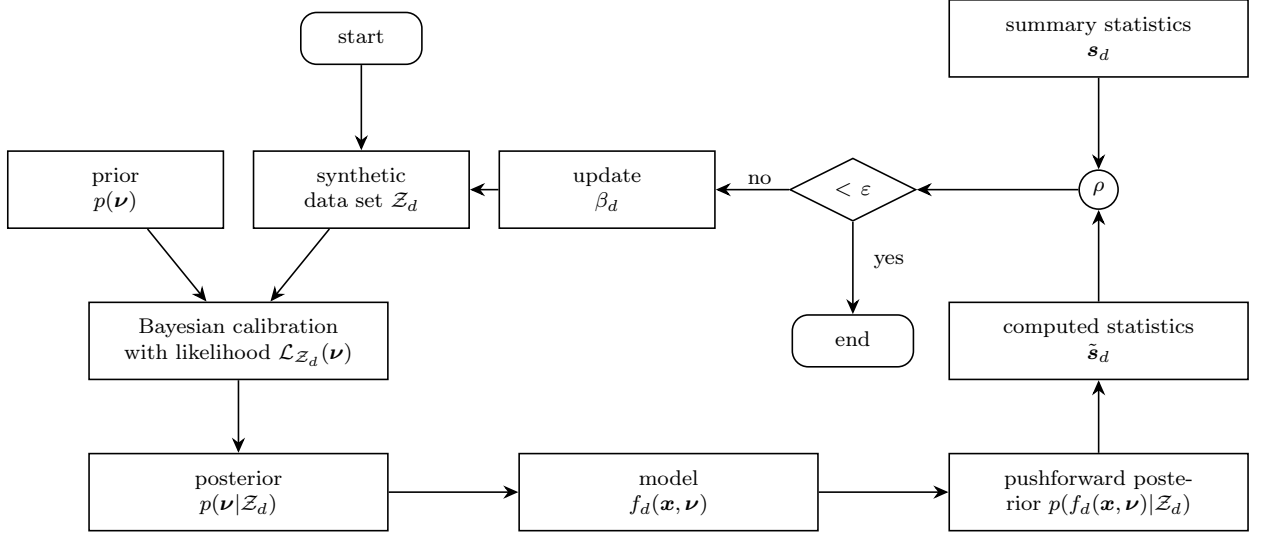


Figure 5: Bayesian calibration framework used to generate a consistent synthetic data set  $\mathcal{Z}_d$  according to [Algorithm 1](#).

what follows, let  $\mathbf{s}_d := \{s_d^{(n)}\}_{n=1}^{N_d}$  be the reported summary statistics in the  $d$ th experiment, and  $\tilde{\mathbf{s}}_d := \{\tilde{s}_d^{(n)}\}_{n=1}^{N_d}$  be the corresponding statistics computed from the pushforward posterior density of the  $d$ th set of experimental data summaries at each measurement location. We may be interested in, for example, the standard deviation of the pushforward posterior, in which case the  $\tilde{s}_d^{(n)}$  may correspond to the sample standard deviations at the measurement stations  $\mathbf{x}_d^{(n)}$ . We define a consistent data set  $\mathcal{Z}_d$  to be a data set that satisfies

$$\rho(\mathbf{s}_d, \tilde{\mathbf{s}}_d) \leq \varepsilon \quad (5)$$

for a given distance metric  $\rho$  and given tolerance  $\varepsilon > 0$ . Consistency may be satisfied by choosing an appropriate value for the scale factor  $\beta_d$  in [\(4\)](#). Hence, a consistent data set can be found by solving a one-dimensional optimization problem where we look for a value of  $\beta_d$  and corresponding data set  $\mathcal{Z}_d$  that generates a pushforward posterior density for which the computed statistics  $\tilde{\mathbf{s}}_d$  satisfy [\(5\)](#). The complete process for generating a consistent data set  $\mathcal{Z}_d$  is given in [Algorithm 1](#) and shown schematically in [Figure 5](#).

In each step of the iterative procedure, we generate a proposed synthetic data set  $\mathcal{Z}_d$  according to [equation \(4\)](#) using the current value of  $\beta_d$ . Next, we set up an inference problem to compute samples from the posterior  $p(\boldsymbol{\nu}|\mathcal{Z}_d)$ . These samples are propagated through the forward model  $f_d(\mathbf{x}, \boldsymbol{\nu})$  for each measurement station  $\mathbf{x}_d^{(n)}$ . After that, we compute the desired statistic from the set of pushed forward samples, and compare the computed statistics to the reported summary statistics. This process is repeated until the statistics extracted from the data are consistent with the reported summary statistics in the sense of [equation \(5\)](#). A crucial step in the algorithm is the update of the scaling factor  $\beta_d$ . Since the computed statistics  $\tilde{\mathbf{s}}_d$  depend on the chosen set of posterior samples, it is a random quantity. Hence, in order for [Algorithm 1](#) to converge, we propose to use a stochastic optimizer to update the value of  $\beta_d$ , see, e.g., [\[42\]](#). However, we find numerically that, in our application, the objective function in [\(5\)](#) changes only mildly with a change in the choice for the set of posterior samples, provided that  $K_d$  and  $M$  in [Algorithm 1](#) are large enough. Therefore, a reasonable approximation for a consistent data set that satisfies [equation \(5\)](#) can be obtained by evaluating the objective function for a set of appropriately-chosen scaling parameters  $\beta_d$ , and by selecting the value of  $\beta_d$  that resulted in the smallest value of  $\rho(\mathbf{s}_d, \tilde{\mathbf{s}}_d)$  across all candidates. This is the strategy we adopt in our numerical results below.

---

**Algorithm 1** Generating consistent data

---

**input:** prior  $p(\boldsymbol{\nu})$ , number of synthetic data sets  $K_d$ , starting value for  $\beta_d$ ,  
MCMC chain starting values  $\boldsymbol{\nu}_0$ , number of MCMC iterations  $M$ , statistic  $w$ ,  
distance metric  $\rho$ , target tolerance  $\varepsilon$ , reported summary statistics  $\mathbf{s}_d$   
**output:** a set of consistent synthetic data sets  $\mathcal{Z}_d^{(k)}$ ,  $k = 1, 2, \dots, K_d$

- 1: **procedure** generate\_consistent\_data( $p(\boldsymbol{\nu}), K_d, \beta_d, \boldsymbol{\nu}_0, M, w, \varepsilon, \mathbf{s}_d$ )
- 2:   **repeat**
- 3:     generate synthetic data  $\mathcal{Z}_d^{(k)}$ ,  $k = 1, 2, \dots, K_d$ , according to [equation \(4\)](#)
- 4:      $\{\boldsymbol{\nu}_m\}_{m=1}^M \leftarrow \text{MCMC}(p(\boldsymbol{\nu}), \mathcal{L}_{\mathcal{Z}_d}(\boldsymbol{\nu}), \boldsymbol{\nu}_0, M)$    // obtain samples from the posterior  $p(\boldsymbol{\nu}|\mathcal{Z}_d)$
- 5:     **for**  $n = 1, 2, \dots, N_d$  **do**   // loop over all measurement stations
- 6:       **for**  $m = 1, 2, \dots, M$  **do**   // loop over all posterior samples
- 7:           $\mathbf{f}_m \leftarrow f(\mathbf{x}_d^{(n)}, \boldsymbol{\nu}_m)$    // evaluate the forward model at the posterior samples
- 8:       **end for**
- 9:        $\tilde{\mathbf{s}}_d^{(n)} \leftarrow w(\mathbf{f}_1, \mathbf{f}_2, \dots, \mathbf{f}_M)$    // compute the desired statistic
- 10:     **end for**
- 11:     update the value for  $\beta_d$
- 12:     **until**  $\rho(\mathbf{s}_d, \tilde{\mathbf{s}}_d) \leq \varepsilon$    // evaluate [equation \(5\)](#)
- 13: **end procedure**

---

### 3.3 Full likelihood construction

Once we have obtained consistent synthetic data sets  $\mathcal{Z}_d$  for each experiment  $d = 1, 2, \dots, D$ , we combine them in a single data set  $\mathcal{Z} = \{\mathcal{Z}_d\}_{d=1}^D$  and set up a final inference problem with log-likelihood

$$\begin{aligned} \log \mathcal{L}_{\mathcal{Z}}(\boldsymbol{\nu}) &:= \sum_{d=1}^D \log \mathcal{L}_{\mathcal{Z}_d}(\boldsymbol{\nu}) \\ &= -\frac{1}{2} \sum_{d=1}^D \sum_{n=1}^{N_d} \left[ \log(2\pi\beta_d s_d^{(n)2}) + \right. \\ &\quad \left. \frac{1}{K_d \beta_d s_d^{(n)2}} \sum_{k=1}^{K_d} \left( z_d^{(n,k)} - f_d(\mathbf{x}_d^{(n)}, \boldsymbol{\nu}) \right)^2 \right]. \end{aligned} \tag{6}$$

It is possible to generalize our proposed likelihood in (6) by using different *weights* for each data set. These weights allow us to express various degrees of confidence in the respective experiments. Suppose we have a set of nonzero positive weights  $\boldsymbol{\alpha} = \{\alpha_d\}_{d=1}^D$  that sum to 1. These weights can be used to update the final log-likelihood as

$$\begin{aligned} \log \mathcal{L}_{\mathcal{Z}, \boldsymbol{\alpha}}(\boldsymbol{\nu}) &:= -\frac{D}{2} \sum_{d=1}^D \alpha_d \sum_{n=1}^{N_d} \left[ \log(2\pi\beta_d s_d^{(n)2}) + \right. \\ &\quad \left. \frac{1}{K_d \beta_d s_d^{(n)2}} \sum_{k=1}^{K_d} \left( z_d^{(n,k)} - f_d(\mathbf{x}_d^{(n)}, \boldsymbol{\nu}) \right)^2 \right]. \end{aligned} \tag{7}$$

We may use these weights, for example, to account for the different number of measurement stations  $N_d$  in each data set. In that case, the weights could be chosen as

$$\alpha_d := \frac{N_d^{-1}}{\sum_{d=1}^D N_d^{-1}}. \tag{8}$$

## 4 Polynomial chaos surrogate construction and parameter reduction

The calibration approach outlined in [Section 3](#) relies heavily on the ability to evaluate the likelihood function  $\mathcal{L}(\boldsymbol{\nu})$  in (6) or (7), and thus also on the ability to evaluate the assumed model  $f_d(\mathbf{x}, \boldsymbol{\nu})$  which, in our setting, is **Centipede**. To avoid excessive computational costs, we propose to use a surrogate model that is inexpensive to evaluate and replaces **Centipede** in the calibration loop. In this work, we focus on *polynomial chaos expansion* (PCE) surrogate models. Given the prohibitively large number of samples required for constructing accurate surrogates in high dimensions, we use a *global sensitivity analysis* (GSA) to identify a reduced set of parameters. This allows us to construct a more accurate surrogate in this lower-dimensional space. The sensitivity analysis will rank the parameters according to their relative effect on the variance of the output, allowing a down-selection based on the fractional contribution of each parameter to the total output variance.

We will briefly recall the PCE surrogate model construction process in [Section 4.1](#), and discuss dimension reduction using GSA in [Section 4.2](#).

### 4.1 Polynomial chaos expansions

A PCE surrogate model  $\tilde{f}_d^{(n)}(\boldsymbol{\nu})$  for the **Centipede** prediction  $f_d(\mathbf{x}_d^{(n)}, \boldsymbol{\nu})$  at measurement station  $\mathbf{x}_d^{(n)}$  can be defined as

$$\tilde{f}_d^{(n)}(\boldsymbol{\nu}) := \sum_{\mathbf{u} \in \mathcal{I}_d^{(n)}} c_{d,\mathbf{u}}^{(n)} \Phi_{\mathbf{u}}(\boldsymbol{\xi}),$$

where  $\mathbf{u} = (u_1, u_2, \dots, u_s) \in \mathbb{N}_0^s$  is a multi-index of length  $s$ ,  $\mathcal{I}_d^{(n)}$  is a set of multi-indices,  $\Phi_{\mathbf{u}}$  is a multivariate orthogonal polynomial expressed in terms of the i.i.d. random variables  $\boldsymbol{\xi} = (\xi_1, \xi_2, \dots, \xi_s)$ , and  $c_{d,\mathbf{u}}^{(n)}$  is a deterministic coefficient that needs to be determined, see, e.g., [\[34, 35, 43–46\]](#). The basis functions  $\Phi_{\mathbf{u}}$  are defined as

$$\Phi_{\mathbf{u}}(\boldsymbol{\xi}) := \prod_{j=1}^s \phi_{u_j}(\xi_j),$$

where  $\phi_{u_j}$  are one-dimensional polynomials of degree  $u_j$ ,  $j = 1, 2, \dots, s$ . By convention, the *order*  $|u|$  of the multivariate polynomial  $\Phi_{\mathbf{u}}$  is given as the sum of all degrees, i.e.,  $|u| := u_1 + u_2 + \dots + u_s$ .

In our numerical experiments in [Section 5](#), and for the purpose of surrogate construction, we define the input parameters  $\nu_j$  as uniformly distributed on  $[a_j, b_j]$ . In this case, the polynomials  $\phi_{u_j}$  are the normalized Legendre orthogonal polynomials, see [\[47\]](#), and the random variables  $\xi_j$  correspond to the model parameter values rescaled to  $[-1, 1]$ , i.e.,

$$\xi_j = 2 \frac{\nu_j - a_j}{b_j - a_j} - 1, \quad j = 1, 2, \dots, s.$$

There are various options for finding the coefficients  $c_{d,\mathbf{u}}^{(n)}$ , as well as the index set  $\mathcal{I}_d^{(n)}$ , based on a set of input-output evaluations, see, e.g., [\[34, 35, 47, 48\]](#). We will use the iterative Bayesian compressive sensing approach outlined in [\[49\]](#).

When evaluating the log-likelihood  $\log \mathcal{L}_{\mathcal{Z}, \boldsymbol{\alpha}}(\boldsymbol{\nu})$  from [equation \(7\)](#), we can now query the computationally cheap surrogate model  $\tilde{f}_d^{(n)}(\boldsymbol{\nu})$  instead of the actual model  $f_d(\mathbf{x}_d^{(n)}, \boldsymbol{\nu})$ , at specific parameter values  $\boldsymbol{\nu}$ . This avoids the need to run **Centipede** in the likelihood evaluation. In particular, the log-likelihood  $\log \mathcal{L}_{\mathcal{Z}, \boldsymbol{\alpha}}(\boldsymbol{\nu})$  can be approximated as

$$\log \mathcal{L}_{\mathcal{Z}, \boldsymbol{\alpha}}^{\text{sur}}(\boldsymbol{\nu}) := -\frac{D}{2} \sum_{d=1}^D \alpha_d \sum_{n=1}^{N_d} \left[ \log(2\pi\beta_d s_d^{(n)2}) + \right.$$

$$\frac{1}{K_d \beta_d s_d^{(n)2}} \sum_{k=1}^{K_d} \left( z_d^{(n,k)} - \tilde{f}_d^{(n)}(\boldsymbol{\nu}) \right)^2 \Big]. \quad (9)$$

## 4.2 Dimension reduction using global sensitivity analysis

A natural way to order the input parameters according to their relative importance is provided through the computation of the Sobol' sensitivity indices, see, e.g., [50]. The Sobol' indices measure fractional contributions of each parameter to the total output variance. The indices can be obtained from a variance-based sensitivity analysis, using a set of randomly-chosen input-output evaluations of the model, see, e.g., [51, 52]. However, when a PCE surrogate model is available, the Sobol' sensitivity indices can be extracted directly from the coefficients of the expansion, exploiting the orthogonality of the basis functions. For example, the *total-effect* Sobol' sensitivity indices are defined as

$$S_{d,j}^{(n)} \approx \frac{\sum_{\mathbf{u} \in \mathcal{J}_{d,j}^{(n)}} c_{d,\mathbf{u}}^{(n)2}}{\sum_{\mathbf{u} \in \mathcal{I}_d^{(n)} \setminus \{\mathbf{0}\}} c_{d,\mathbf{u}}^{(n)2}}, \quad (10)$$

with  $\mathcal{J}_{d,j}^{(n)} = \{\mathbf{u} \in \mathcal{I}_d^{(n)} : u_j > 0\}$ . The total-effect sensitivity index is a measure of sensitivity describing which share of the total variance of the model output can be attributed to the  $j$ th parameter, including its interaction with other input variables [50]. Parameters with small total-effect indices have an overall small contribution to uncertainty in model outputs, and can thus be treated as deterministic, thereby decreasing the dimensionality of the uncertain input space, and the corresponding dimensionality of the surrogate. Having constructed a PCE surrogate model, one can easily evaluate the sensitivity indices by gathering the (square of the) appropriate coefficients. Note that

$$\sum_{j=1}^s S_{d,j}^{(n)} \geq 1,$$

due to the fact that the interaction effects are counted multiple times in the index set  $\mathcal{J}_{d,j}^{(n)}$ .

## 5 Results and discussion

In this section, we present our main results obtained by using the calibration framework outlined in [Sections 3](#) and [4](#) to estimate the parameters of **Centipede**. Overall, our calibration strategy consists of three steps:

1. First, we create a set of PCE surrogates for **Centipede** in the full, 183-dimensional parameter space. We use GSA to identify a set of 24 important parameters.
2. Next, we reconstruct the set of PCE surrogates in the reduced, 24-dimensional parameter space. These surrogates are more accurate, and can be used to replace the actual **Centipede** predictions in the evaluation of the likelihood.
3. Finally, we generate a consistent synthetic data set for each experiment, and use these data sets to perform Bayesian calibration using both the unweighted and weighted likelihood formulations.

The remainder of this section is organized as follows. First, in [Section 5.1](#), we provide more details on the experimental setup. Afterwards, in [Sections 5.2](#) to [5.4](#), we discuss the three steps of our calibration strategy in more detail. The result of the calibration effort is reported in [Sections 5.5](#) and [5.6](#), and a discussion of these results is provided in [Section 5.7](#).

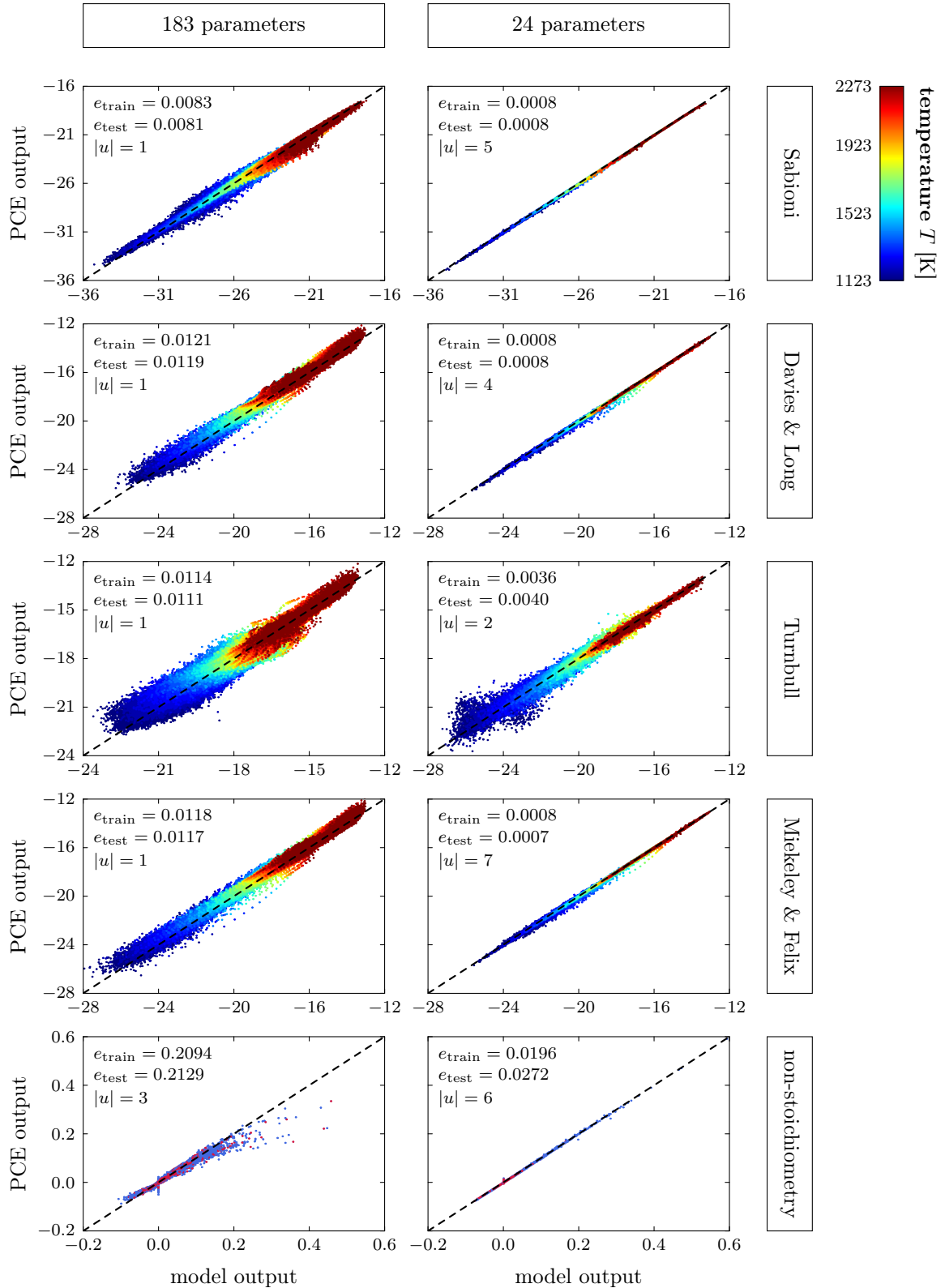


Figure 6: Comparison of the predicted outputs from the PCE surrogate model and the actual model outputs for the quantity predicted by each set of data summaries for the 183-parameter model (*left column*) and the 24-parameter model (*right column*). We indicate the relative training error  $e_{\text{train}}$ , the relative test error  $e_{\text{test}}$ , and the order of the PCE  $|u|$  for the surrogate with the largest relative test error across all (combinations of) temperatures (and  $p_{\text{O}_2}$  values). For the diffusivity predictions (first 4 rows), different colors indicate different temperatures, and for the non-stoichiometry predictions (last row), we distinguish between training (*blue*) and test samples (*red*).

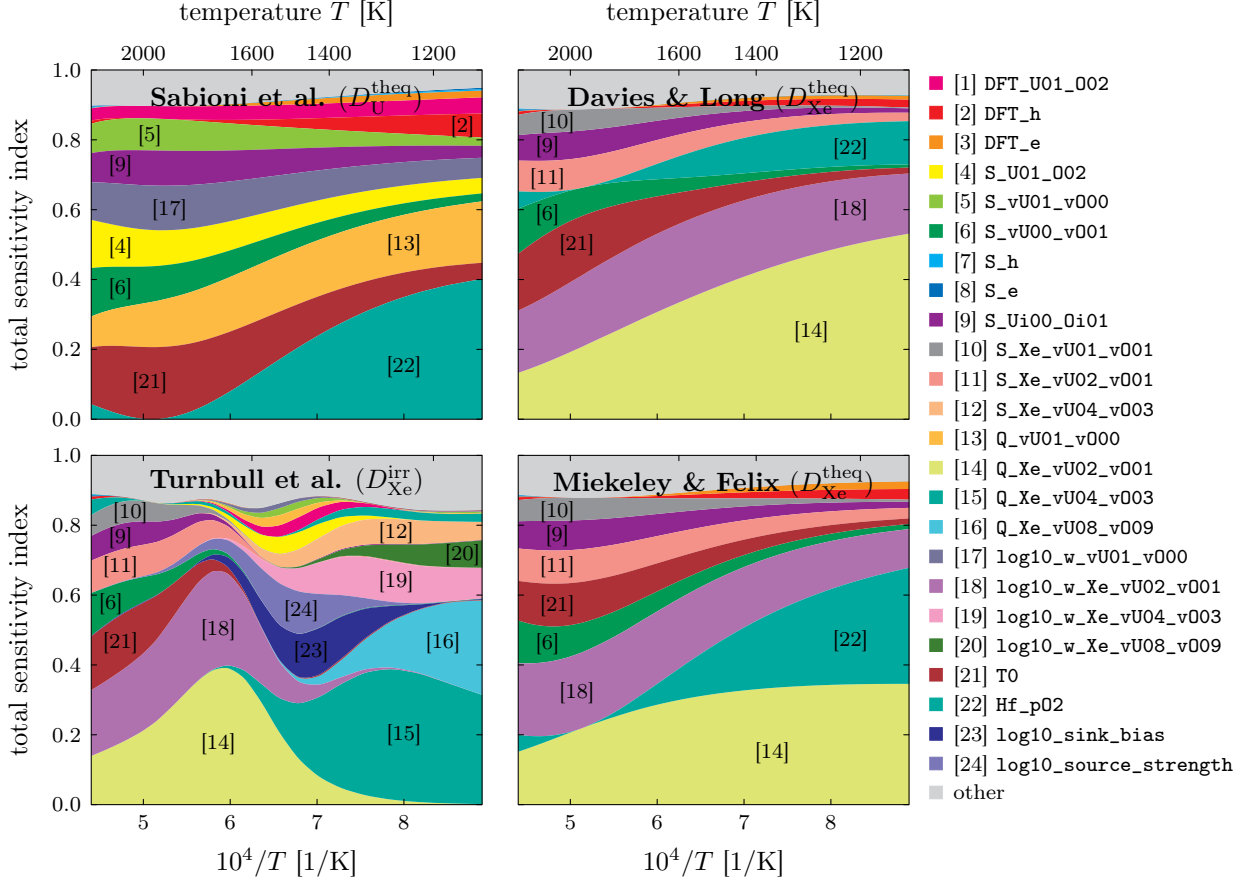


Figure 7: Total-effect Sobol' sensitivity indices of the diffusivity predictions in each experiment as a function of temperature. Only the sensitivity indices of the 24 most important parameters are included. Different colors correspond to different parameters.

## 5.1 Experimental setup

**Centipede** implements the Free Energy Cluster Dynamics (FECDD) method from [18] within the MOOSE framework [53]. MOOSE provides access to the Finite Element code `libMesh` [54], and the partial differential equation (PDE) solver `PETSc` [55]. The latter is a crucial component for the efficient solution of the system of nonlinear ODEs in (1) that represent the cluster dynamics physics.

The uranium and xenon diffusivities under thermal equilibrium,  $D_U^{\text{theq}}$  and  $D_{\text{Xe}}^{\text{theq}}$ , and xenon diffusivity under irradiation conditions,  $D_{\text{Xe}}^{\text{irr}}$ , vary with temperature. The **Centipede** predictions of these diffusivities are available at a set of 26 temperatures provided in Table 3. These temperatures span the range of experimental conditions where the data summaries are available. Evaluating **Centipede** at all temperatures where the data summaries are available would lead to excessive computational requirements, as one would have to solve equation (1) at each temperature. Consequentially, the PCE surrogate model predictions for the uranium and xenon diffusivities will be available only at these 26 temperatures. Since the evaluation of the likelihood in equation (9) requires access to a set of surrogate models  $f_d^{(n)}$ ,  $n = 1, 2, \dots, N_d$  defined at each temperature  $\mathbf{x}_d^{(n)}$ , we propose to use a suitable interpolation scheme. In what follows, we assume a linear interpolation scheme, and remark that linear interpolation of the PCE outputs can be accomplished by linear interpolation of the PCE coefficients.

The fuel non-stoichiometry  $\text{UO}_{2\pm x}$  is a function of both  $T$  and  $p_{\text{O}_2}$ . **Centipede** predictions for  $\text{UO}_{2\pm x}$  are available at the same 104 combinations of  $T$  and  $p_{\text{O}_2}$  where the data summaries are available, so no interpolation of the PCE surrogate models is required in this case.

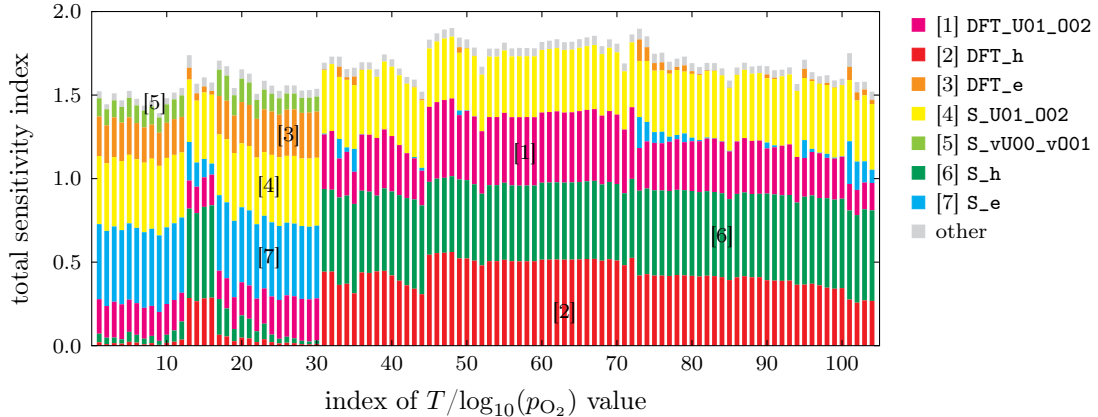


Figure 8: Total-effect Sobol’ sensitivity indices of the non-stoichiometry predictions  $\text{UO}_{2\pm x}$  as a function of the  $T/\log_{10}(p_{\text{O}_2})$  index. We only included the 12 thermodynamic parameters in the sensitivity analysis, as the kinetic parameters have no effect on the non-stoichiometry predictions. Only the sensitivity indices of the 7 most important parameters are shown. Different colors correspond to different parameters. Indices 1–30 correspond to stoichiometric predictions at high temperatures and low  $p_{\text{O}_2}$ , while indices 31–104 correspond to low temperatures and high  $p_{\text{O}_2}$ .

As indicated in Table 1, the operating conditions  $\text{Hf\_pO2}$  and  $T_0$  are unique for each experiment that predicts the diffusivity quantities. As such, we will allow them to vary independently. This can be achieved by enriching the set of parameters used in the calibration with experiment-specific copies of these operating conditions. This increases the number of parameters to calibrate from 24 to 30.

The lower bounds  $a_j$  and upper bounds  $b_j$  used to construct the PCE surrogate models are defined in Table 9. The PCE surrogates and subsequent sensitivity analysis are performed using the uncertainty quantification toolkit (UQTK), see [48, 56]. We also implemented the DFI method outlined in Section 3.1 in UQTK.

We remark that not all parameter combinations yield valid output samples of the stoichiometry and/or diffusivity, due to a lack of convergence of the underlying ODE solver, or because the sampled set of parameters resulted in unphysical responses. In our experiments, the number of code failures is about 3% for the 183-parameter model, and 2% for the 24-parameter model. These code failures seem to happen because of convoluted interaction effects between parameters, as we were unable to attribute the failures to certain regions of the parameter space. A careful analysis of these code failures is left for future work.

During calibration, we employ Gaussian priors on these parameters,

$$p(\boldsymbol{\nu}) = \prod_{j=1}^s p(\nu_j)$$

with

$$p(\nu_j) \sim \mathcal{N}\left(\frac{a_j + b_j}{2}, \frac{(b_j - a_j)^2}{36}\right).$$

This choice means that 99% of the probability mass of the prior is contained between the given lower and upper bounds.

## 5.2 Surrogate construction and sensitivity analysis

For the uranium and xenon diffusivities, we construct a set of first-order PCE surrogate models in 183 dimensions, one for each of the 26 temperatures. Similarly, for the stoichiometry predictions,

Sabioni et al.	Davies & Long	Turnbull et al.	Miekeley & Felix	non-stoichiometry
Hf_p02	Q_Xe_vU02_v001	Q_Xe_vU02_v001	Q_Xe_vU02_v001	DFT_h
TO	log10_w_Xe_vU02_v001	Q_Xe_vU04_v003	Hf_p02	S_h
Q_vU01_v000	TO	log10_w_Xe_vU02_v001	log10_w_Xe_vU02_v001	DFT_U01_002
S_vU00_v001	S_vU00_v001	Q_Xe_vU08_v009	S_vU00_v001	S_e
S_U01_002	Hf_p02	TO	TO	S_U01_002
log10_w_vU01_v000	S_Xe_vU02_v001	log10_sink_bias	S_Xe_vU02_v001	DFT_e
S_Ui00_0i01	S_Ui00_0i01	S_vU00_v001	S_Ui00_0i01	S_vU00_v001
S_vU01_v000	S_Xe_vU01_v001	log10_source_strength	S_Xe_vU01_v001	DFT_vU00_v001
DFT_h	DFT_vU00_v001	log10_w_Xe_vU04_v003	DFT_vU00_v001	S_U01_v000
DFT_U01_002	DFT_Xe_vU02_v001	S_Xe_vU02_v001	DFT_Xe_vU02_v001	DFT_vU01_v000
DFT_vU00_v001	DFT_Ui00_0i01	log10_w_Xe_vU08_v009	DFT_Ui00_0i01	S_Ui00_0i01
DFT_vU01_v000	DFT_h	S_Ui00_0i01	DFT_h	DFT_Ui00_0i01
DFT_Ui00_0i01	DFT_Xe_vU01_v001	S_Xe_vU04_v003	DFT_Xe_vU01_v001	
DFT_e	DFT_Xe_vU02_v002	S_Xe_vU01_v001	DFT_e	
S_h	S_Xe_vU02_v002	log10_sink_strength	DFT_Xe_vU02_v002	
S_e	DFT_e	DFT_Xe_vU04_v003	S_Xe_vU02_v002	
Q_vU01_v002	S_e	S_U01_002	S_e	
S_vU01_v002	S_h	Hf_p02	S_h	
log10_w_vU01_v002	S_Xe_vU01_v002	DFT_vU00_v001	charge_correction_DFT	
charge_sq_correction_DFT	charge_correction_DFT	DFT_Xe_vU04_v002	S_Xe_vU01_v002	
DFT_vU01_v002	charge_sq_correction_DFT	DFT_U01_002	charge_sq_correction_DFT	
charge_correction_DFT	DFT_Xe_vU01_v002	S_Xe_vU02_v002	DFT_Xe_vU01_v002	
Q_vU02_v002	DFT_vU01_v000	S_Xe_vU04_v002	Q_Xe_vU02_v002	
S_vU02_v002	Q_Xe_vU02_v002	DFT_Xe_vU02_v001	log10_w_Xe_vU02_v002	
log10_w_vU02_v002	Q_Xe_vU02_v000	Q_vU01_v000	log10_sink_bias	
log10_w_vU02_v001	log10_w_Xe_vU02_v002	DFT_Ui00_0i01	DFT_Xe_vU02_v000	
Q_vU02_v000	Q_Xe_vU04_v003	S_vU01_v000	S_vU01_v000	
DFT_vU02_v002	S_vU01_v000	DFT_Xe_vU01_v001	log10_w_Xe_Ui01_0i00	
S_vU02_v001	DFT_Xe_vU02_v000	DFT_Xe_vU02_v002	log10_sink_strength	
Q_vU02_v001	log10_w_Xe_vU02_v000	log10_w_vU01_v000	log10_w_Xe_vU02_v000	
⋮	⋮	⋮	⋮	

Table 2: Parameters of **Centipede** ordered according to their maximum Sobol’ total sensitivity index across all temperatures and  $p_{O_2}$  values for each experiment. Different colors indicate which parameters will be retained when we want to capture a certain percentage of the total output variance: 70% (■, 21 parameters), 75% (■ + ■, 24 parameters), 80% (■ + ■ + ■, 26 parameters), 85% (■ + ■ + ■ + ■, 28 parameters), 90% (■ + ■ + ■ + ■ + ■, 31 parameters), 95% (■ + ■ + ■ + ■ + ■ + ■, 33 parameters), 99% (■ + ■ + ■ + ■ + ■ + ■ + ■, 35 parameters).

we construct a higher-order PCE surrogate model at each combination of  $T$  and  $p_{O_2}$  where the data  $\mathcal{D}_5$  is available. These surrogates are built using 10,000 input-output evaluations of **Centipede** as training data, and 1,000 evaluations as test data. The input training and test data is sampled from a uniform distribution between the given lower bounds  $a_j$  and upper bounds  $b_j$  for each parameter  $j = 1, 2, \dots, 183$ . During the construction of the higher-order surrogates for the non-stoichiometry ( $UO_{2\pm x}$ ), we used the adaptive procedure described in [49]. We illustrate the accuracy of these PCE surrogate models by comparing the predicted outputs from the surrogate with the actual model outputs in the left column of **Figure 6**. Each point in this figure represents a single sample. The surrogate model outputs are in perfect agreement with the **Centipede** outputs if all points fall on the diagonal (*dashed line*). In the plots, we indicate the relative  $\ell_2$  training error,  $e_{\text{train}}$ , where

$$e_{\text{train}}^2 = \frac{\sum_{l=1}^{L_{\text{train}}} \sum_{n=1}^{N_d} \left( f_d^{(n)}(\boldsymbol{\nu}_{\text{train}}^{(l)}) - \tilde{f}_d^{(n)}(\boldsymbol{\nu}_{\text{train}}^{(l)}) \right)^2}{\sum_{l=1}^{L_{\text{train}}} \sum_{n=1}^{N_d} f_d^{(n)}(\boldsymbol{\nu}_{\text{train}}^{(l)})^2} \quad (11)$$

and  $\boldsymbol{\nu}_{\text{train}}^{(l)}$ ,  $l = 1, 2, \dots, L_{\text{train}}$  are the training samples. We also indicate the test error  $e_{\text{test}}$ , defined similar to **equation (11)**, and the order of the PCE  $|u|$  corresponding to the surrogate with largest relative test error across all (combinations of) temperatures (and  $p_{O_2}$  values). Note that, because training and test errors are relatively close, we conclude that the PCE surrogate models do not suffer from overfitting. Also note that the accuracy of these 183-dimensional surrogates is poor. The accuracy of the surrogate models for the non-stoichiometry ( $UO_{2\pm x}$ ) seems particularly low, despite the higher-order construction scheme. This accuracy concern could be addressed by increasing the number of training samples  $L_{\text{train}}$ , causing a consequential growth in the computational requirements. However, we deem the accuracy of the surrogates to be sufficient for the estimation of sensitivity indices.

With these surrogates available, we are able to evaluate the sensitivity indices using **equa-**

tion (10). The result is shown in [Figure 7](#) for the diffusivity predictions, and [Figure 8](#) for the stoichiometry predictions.

[Figure 7](#) shows the total Sobol’ sensitivity indices for the diffusivity quantities as a function of temperature. Different colors indicate different parameters, and the parameters are ordered according to their maximum sensitivity index across all temperatures, for the 24 most important parameters only. Note that the names of these parameters correspond to the internal labelling used by `Centipede`, see also [Table 9](#). The light gray area on top of each axis represents the fraction of unexplained output variance.

For  $D_U^{\text{theq}}$ , predicted by Sabioni et al., the three most important parameters are `Hf_p02`, `T0`, and the activation energy of uranium (`Q_vU01_v000`), which is consistent with the active uranium vacancy diffusion mechanism identified in [19]. It is interesting to note that out of the three most impactful parameters, two refer to the operating conditions of the experiment, and only one refers to the specific properties of uranium vacancies. As expected for a thermal equilibrium experiment on uranium diffusion only, none of the sensitive parameters refers to the response due to irradiation or the properties of xenon.

For  $D_{\text{Xe}}^{\text{theq}}$ , predicted by Davies & Long, the three most important parameters are the activation energy of xenon in the  $\text{U}_2\text{O}$  cluster (`Q_Xe_vU02_v001`), the (log of the) attempt frequency of xenon in the  $\text{U}_2\text{O}$  vacancy cluster (`log10_w_Xe_vU02_v001`), and `T0`. Again, these parameters are consistent with the active diffusion mechanism previously identified, and also emphasize the impact of the thermodynamic conditions of the experiment, which govern the non-stoichiometry  $\text{UO}_{2\pm x}$ .

For  $D_{\text{Xe}}^{\text{irr}}$ , predicted by Turnbull et al., the three most important parameters are `Q_Xe_vU02_v001`, the activation energy of the xenon defect located at a  $\text{U}_4\text{O}_3$  vacancy cluster (`Q_Xe_vU04_v003`), and `log10_w_Xe_vU02_v001`. It is worth pointing out that the significance of  $\text{Xe}_{\text{U}_4\text{O}_3}$ , i.e., the xenon defect located at the  $\text{U}_4\text{O}_3$  vacancy cluster, as well as the significance of  $\text{Xe}_{\text{U}_8\text{O}_9}$ , which appears in the list of important parameters through the activation energy of the xenon defect located at  $\text{U}_8\text{O}_9$  (`Q_Xe_vU08_v009`), has been speculated in [8], and is confirmed in our sensitivity analysis. In particular, in previous studies,  $\text{Xe}_{\text{U}_2\text{O}}$  was identified as being responsible for diffusion at high temperature, and  $\text{Xe}_{\text{U}_4\text{O}_3}$  was identified as being responsible for diffusion at intermediate temperatures, and, although  $\text{Xe}_{\text{U}_8\text{O}_9}$  was not predicted to be the main contributor to diffusion in previous studies, it was close to the dominant  $\text{Xe}_{\text{U}_4\text{O}_3}$  cluster in the intermediate temperature range, see [19]. The change in sensitivity as a function of temperature in [Figure 7](#) confirms these observations. It also emphasizes the competition between  $\text{Xe}_{\text{UO}}$  and  $\text{Xe}_{\text{U}_2\text{O}}$  at high temperatures, and the transition from thermodynamic parameters (`T0`) to irradiation parameters (`log10_sink_bias` and `log10_source_strength`) with decreasing temperature.

For  $D_{\text{Xe}}^{\text{theq}}$ , predicted by Miekeley & Felix, the three most important parameters are `Q_Xe_vU02_v001`, `Hf_p02`, and `log10_w_Xe_vU02_v001`. Although the exact ordering of the parameters is slightly different from the results reported for  $D_{\text{Xe}}^{\text{theq}}$  predicted by Davies & Long, the parameter set is very similar, which is expected based on the fact that both data sets predict xenon diffusion under thermal equilibrium conditions. However, we expect that the operating conditions may differ between the two experiments, due to the difference in experimental setup.

[Figure 8](#) shows the total Sobol’ sensitivity indices for the non-stoichiometry  $\text{UO}_{2\pm x}$  as a function of the  $T/\log_{10}(p_{\text{O}_2})$  index. Again, different colors indicate different parameters, and the parameters are ordered according to their maximum sensitivity index across all indices. Note that, in our sensitivity analysis, we took into account that the non-stoichiometry depends only on the 12 thermodynamic parameters, and not on the kinetic parameters that influence the diffusivities. Only those thermodynamic parameters that are part of the set of 24 most important parameters overall are included in the plot. The three most important parameters for the stoichiometric predictions at high temperatures and low partial pressure (indices 1 – 30) are the entropy of the electrons (`S_e`), the entropy of  $\text{UO}_2$  (`S_U01_002`), and the electron formation energy (`DFT_e`). The three most important parameters for the stoichiometric predictions at low temperatures and high partial pressure (indices 31 – 104) are the formation energy of the holes (`DFT_h`), the entropy of the holes (`S_h`) and

the formation energy of  $\text{UO}_2$  (DFT\_U01\_002). Also note that the sum of the total sensitivity indices is larger than 1, indicating that there are significant interaction effects between the thermodynamic parameters.

Finally, we note that the parameters in the correction terms for the binding energies (i.e., `charge_correction_DFT` and `charge_sq_correction_DFT`), that account for systematic errors in the binding energies, are unimportant for all quantities of interest.

### 5.3 Dimension reduction

The total sensitivity indices allow us to rank the 183 parameters according to their contribution to the output variance. By assuming a prescribed fraction of the output variance that needs to be explained across all  $D = 5$  data sets, we can obtain a sequence of reduced models that contain subsets of all 183 parameters. This truncation strategy is illustrated in [Table 2](#). Ensuring that at least 75% of the output variance is captured for each predicted quantity, we identify a set of 24 important parameters. Note that the actual fraction of the variance explained for each predicted output individually is slightly larger than the threshold of 75%. That is, the set of required parameters to reach the prescribed threshold in output variance explained for each experiment is a subset of the 24 chosen parameters. By including additional parameters, the overall fraction of variance explained increases beyond that threshold. In particular, the fraction of output variance explained using our reduced set of 24 parameters is 90% (Sabioni et al.), 87% (Davies & Long), 84% (Turnbull et al.), and 88% (Miekeley & Felix).

Next, we reconstruct the PCE surrogates for both the diffusivity and non-stoichiometry predictions a second time, now using only 24 uncertain parameters, keeping the 159 parameters that were excluded by the sensitivity analysis at their nominal value. Using approximately 25,000 and 2,500 input-output evaluations of `Centipede` as training and test data, respectively, we construct a set of higher-order PCE surrogates using the iterative procedure described in [\[49\]](#). As before, the input training and test data is sampled from uniform distributions between the lower and upper bounds given in [Table 9](#) for the 24 uncertain parameters. To assess the accuracy of these new PCE surrogates, we compare the predicted outputs from the surrogate with the actual model outputs in the right column of [Figure 6](#). We also indicate training and test errors computed using [\(11\)](#). Because the training and test errors are similar, we again conclude that the surrogates are not overfitted. These results clearly indicate the improved surrogate accuracy in the 24-dimensional context, as compared to the 183-dimensional surrogate.

### 5.4 Generating consistent synthetic data sets

The first step in our calibration framework outlined in [Section 3](#) is the generation of consistent synthetic data sets. Having prescribed the synthetic data sets as in [equation \(4\)](#), this requires us to find an appropriate value for the scaling factor  $\beta_d$  in the variance of the data-generating distribution. These scaling factors can be found by matching the statistics of the pushforward posterior  $\tilde{\mathbf{s}}_d$ , to the given measurement errors  $\mathbf{s}_d$ , such that the criterion in [\(5\)](#) is satisfied. In our experiments, we will use the  $3\sigma$  statistic of the pushforward posterior, and use the relative  $\ell_2$  norm as distance metric. We evaluate the statistics  $\tilde{\mathbf{s}}_d$  for each data set  $d = 1, 2, \dots, D$  based on samples from the pushforward posterior, obtained by MCMC, with the log-pooled likelihood defined in [equation \(9\)](#). We use a total of  $M = 10^6$  MCMC steps,  $K = 100$  synthetic data sets, a proposal jump size of 0.5, and evaluate the pushforward posterior with a burn-in of 100 000 and subsampling rate of 5, i.e., we keep 1 out of every 5 samples in order to decorrelate the Markov chain. In order to obtain good starting values for the chain, we performed a few iterations with the deterministic optimization method L-BFGS, see [\[57\]](#). We evaluate the metric in [\(5\)](#) for a set of 20 judiciously chosen values of the scaling factor  $\beta_d$ .

The values of  $\|\mathbf{s}_d - \tilde{\mathbf{s}}_d\|_2$  as a function of  $\beta_d$  are reported in [Figure 9](#). Note that, in order to generate these plots, we fixed the random seeds used to generate the synthetic data set  $\mathcal{Z}_d$  for

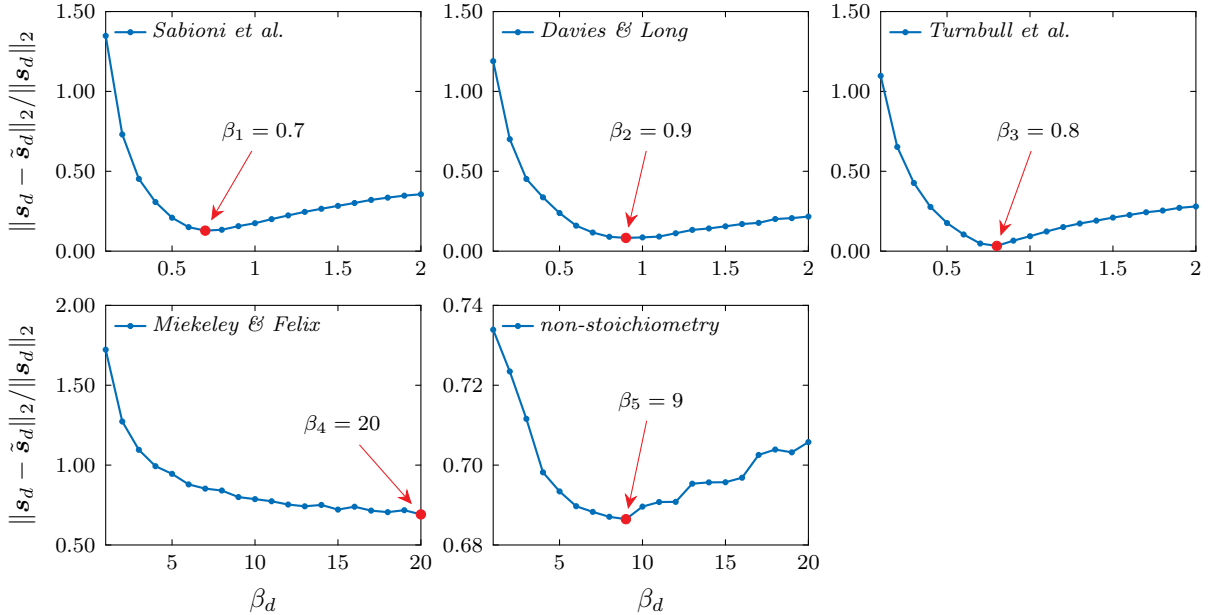


Figure 9: Relative  $\ell_2$ -norm of the difference between the reported summary statistics  $\mathbf{s}_d$  and the computed summary statistics from the pushforward posterior  $\tilde{\mathbf{s}}_d$  as a function of the synthetic data scaling parameter  $\beta_d$  for each set of experimental data summaries. The computed summary statistics  $\tilde{\mathbf{s}}_d$  correspond to three times the standard deviation ( $3\sigma$ ). Values of the scaling parameter  $\beta_d$  used in the final calibration are indicated by  $\bullet$ .

various choices of  $\beta_d$ , because we found numerically that this provides slightly more stable results, and  $K = 100$  synthetic data sets appears to be sufficient to avoid any significant difference in the pushforward posterior predictions due to variations in the number of synthetic data sets  $K$ . For each experiment, except Miekeley & Felix, there is a well-defined optimum, where the difference between the reported measurement errors and the  $3\sigma$  statistic of the pushforward posterior are in good agreement. For the Miekeley & Felix experiment, the relative error between the predicted statistics and the reported data summaries is large, and this does not seem to improve by including even larger values of  $\beta_d$ . This can probably be explained by the relatively large values of the reported uncertainties.

## 5.5 Calibration results

We combine the 5 consistent synthetic data sets  $\mathcal{Z}_d$  obtained in Section 5.4 into a single synthetic data set  $\mathcal{Z} = \{\mathcal{Z}_d\}_{d=1}^5$ . This allows us to construct the full posterior  $p(\boldsymbol{\nu}|\mathcal{Z})$  using MCMC, with a log-likelihood given by equation (9), assuming  $\alpha_d = 1$ ,  $d = 1, 2, \dots, D$ . As before, we use a total of  $M = 10^6$  MCMC steps, a proposal jump size of 0.5, and obtain samples from the posterior assuming a burn-in of 100 000 and subsampling rate of 5. A trace plot of the Markov chain illustrating good mixing is shown in Figure 15.

In Figure 10, we plot the pushforward posterior of the diffusivity quantities, obtained by evaluating the PCE surrogates for the diffusivities in the posterior samples. We indicate the mean (*full line*), standard deviation (*dark shaded area*), and three times the standard deviation (*light shaded area*) of the pushforward posterior, as well as the pushforward *maximum a posteriori* (MAP) prediction (*dashed line*). The MAP values represent the most probable parameter values after the parameter estimation procedure. Diffusivity predictions using the nominal parameter values from [19] are indicated by the *dotted line*. Note that the mean of the pushforward posterior as well as the MAP prediction are in better agreement with the majority of the experimental data summaries than predictions with the original nominal parameters, confirming the efficacy of our calibration framework.

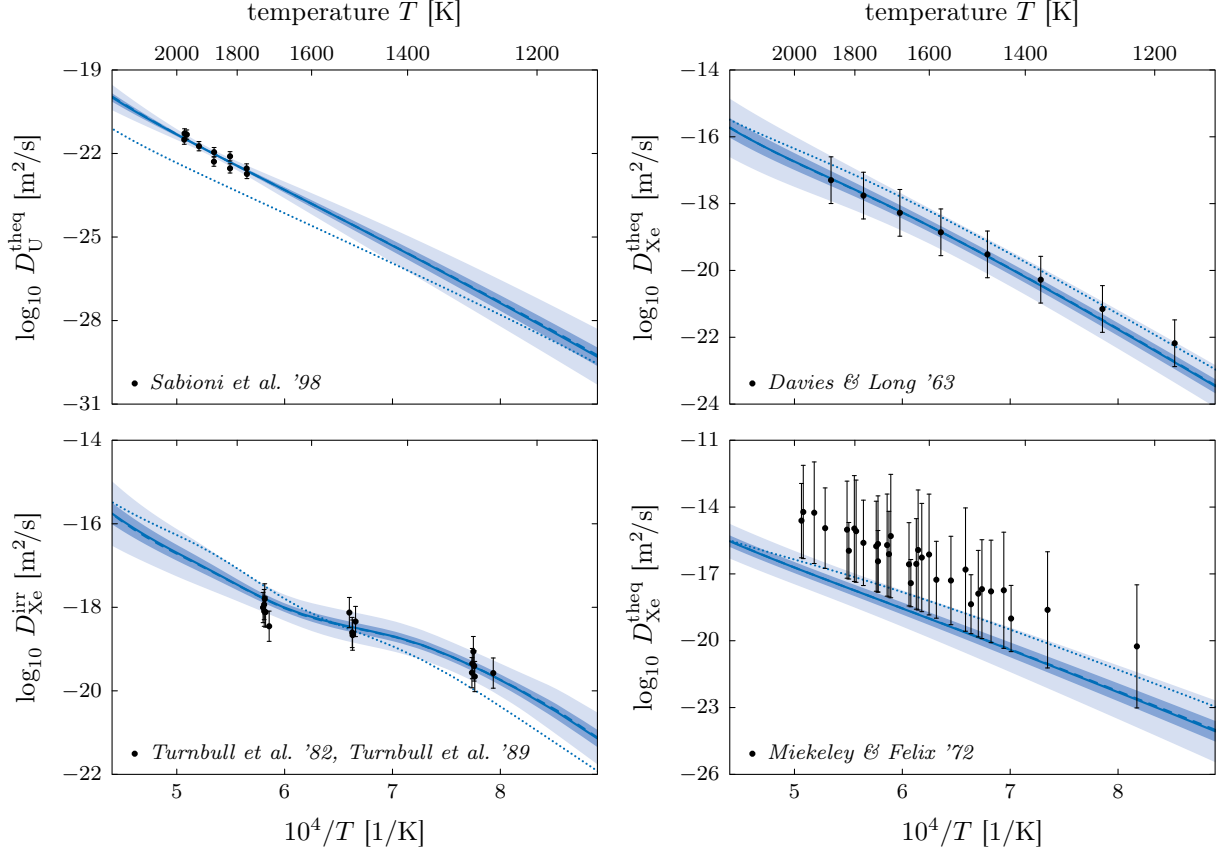


Figure 10: Mean value (*solid line*), mean value  $\pm$  standard deviation (*dark shaded area*), mean value  $\pm$  three times the standard deviation (*light shaded area*), and MAP (*dashed line*) of the pushforward posterior predictions for  $D_U^{\text{theq}}$ ,  $D_{\text{Xe}}^{\text{theq}}$ ,  $D_{\text{Xe}}^{\text{irr}}$  at the particular operating conditions corresponding to each experiment. We also indicate the diffusivity predictions using the nominal parameter values (*dotted line*) from [19]. The data summaries are shown as error bars for comparison.

Furthermore, the  $\pm 3\sigma$  statistic of the pushforward posterior is in good agreement with the reported uncertainties in the majority of the data summaries, as desired. Notably, for the Miekeley & Felix data set (*bottom right*), there is a discrepancy between the pushforward posterior prediction and the data summaries. This is in agreement with our expectations, as we deem the Miekeley & Felix experiment to be slightly less reliable. Alternatively, it is possible that the conditions of this experiment are sufficiently different from the assumed approximately stoichiometric  $\text{UO}_2$  conditions in **Centipede**, such that new diffusion mechanisms involving, for example, different cluster charge states could be activated. **Centipede** would not be able to capture such behavior. The present study helps to identify this issue, and points to potential directions for model improvement.

Similarly, **Figure 11** shows a comparison between the pushforward posterior of the non-stoichiometry ( $\text{UO}_{2\pm x}$ ) and the reported summary statistics. We note that there is a reasonable agreement between both. Our results indicate that the  $3\sigma$  statistic of the non-stoichiometry is strongly dependent on the value of  $T$  and  $p_{\text{O}_2}$ . However, the reported data summaries appear to have mostly constant uncertainties.

## 5.6 Effect of weights in the likelihood

Next, we investigate the effect of weights in the likelihood to compensate for the number of measurements in each reported set of data summaries. To this end, we repeat the calibration with a weighted likelihood, where weights are chosen according to **equation (8)**. We compare the obtained marginal posterior densities on the parameters for both the unweighted and weighted likelihoods in

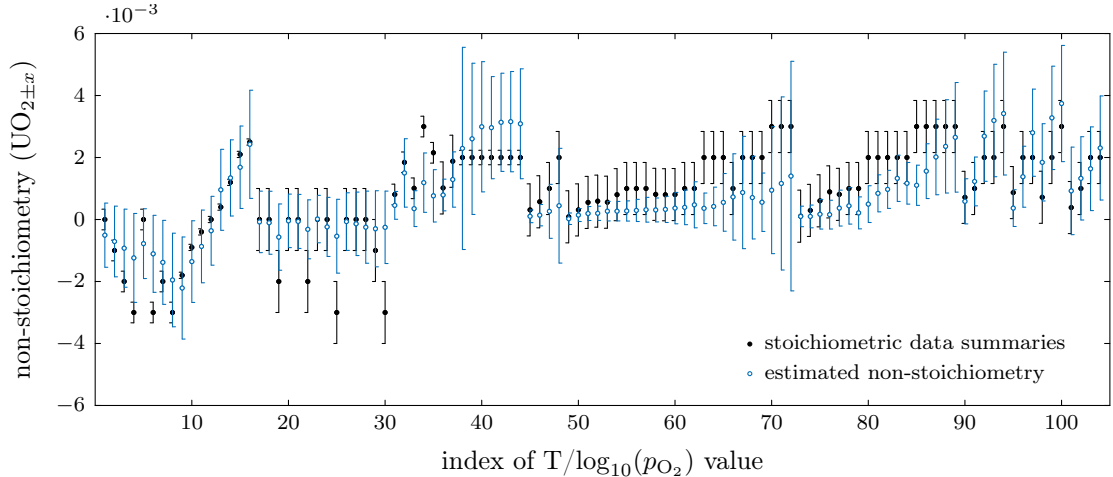


Figure 11: Mean and standard deviation of the pushforward posterior predictions for  $x$  in  $\text{UO}_{2\pm x}$  shown as error bars (*hollow markers*). The data summaries are shown as error bars (*full markers*) for comparison.

**Figure 12.** Overall, the marginal posteriors are in good agreement, although there are some quantitative differences for the formation energy of  $\text{UO}_2$  and the attempt frequencies of  $\text{XeU}_2\text{O}$ ,  $\text{XeU}_4\text{O}_3$  and  $\text{XeU}_8\text{O}_9$ . The numerical values of the MAP predictions of each parameter in the unweighted and weighted case have been included in [Table 10](#).

## 5.7 Discussion

In [Figure 13](#), we compare the pushforward MAP prediction of the xenon diffusivity under irradiation conditions computed using the surrogate (*full line*) with the pushforward MAP prediction computed using **Centipede** (*dotted line*), for the unweighted (*left*) and weighted (*right*) posterior, and using the particular values for the operating conditions estimated for the Turnbull et al. experiments. We also show the Turnbull et al. experimental data summaries for the xenon diffusivity under irradiation conditions, and the Davies & Long experimental data summaries for the intrinsic xenon diffusivity, together with the Turnbull et al. fit from [\[9\]](#) (*dashed line*). The Turnbull et al. fit for xenon diffusion consists of two terms, a  $D_1$  contribution from Davies & Long and a  $D_2$  contribution from Turnbull et al., see [Figure 1](#), and is commonly used in the literature, because it gives good results for integral fuel rod tests (not shown here), and because it captures the Davies & Long and Turnbull et al. data that was used to rationalize its form.

The surrogate prediction with the MAP parameters, as well as the corresponding **Centipede** prediction, are in excellent agreement with the Turnbull fit for temperatures above 1600 K. The fit is slightly worse for low temperatures because the athermal  $D_3$  term contributing to diffusion below about 1200 K is not predicted by **Centipede** (note that we preprocessed the Turnbull et al. data, as well as the fit from the data, to remove the athermal  $D_3$  term). The excellent agreement of the calibrated diffusivity with the (extrapolation of the) Davies & Long data is a consequence of the estimated operating conditions for the Davies & Long data ( $T_0 \approx 2070.1338$  K and  $\text{Hf\_p02} \approx 5.0941$  eV in the weighted setting) being very similar to those estimated for the Turnbull et al. data ( $T_0 \approx 1942.0619$  K and  $\text{Hf\_p02} \approx 5.1278$  eV in the weighted setting).

[Figure 14](#) shows the contributions of the individual defects to the xenon diffusivity under irradiation, for the 10 most important defects, for both the nominal parameter values (*left*) and the estimated parameters using the weighted likelihood formulation (*right*). These plots confirm the vacancy-based mechanism for xenon diffusion that was previously identified in [\[19\]](#).

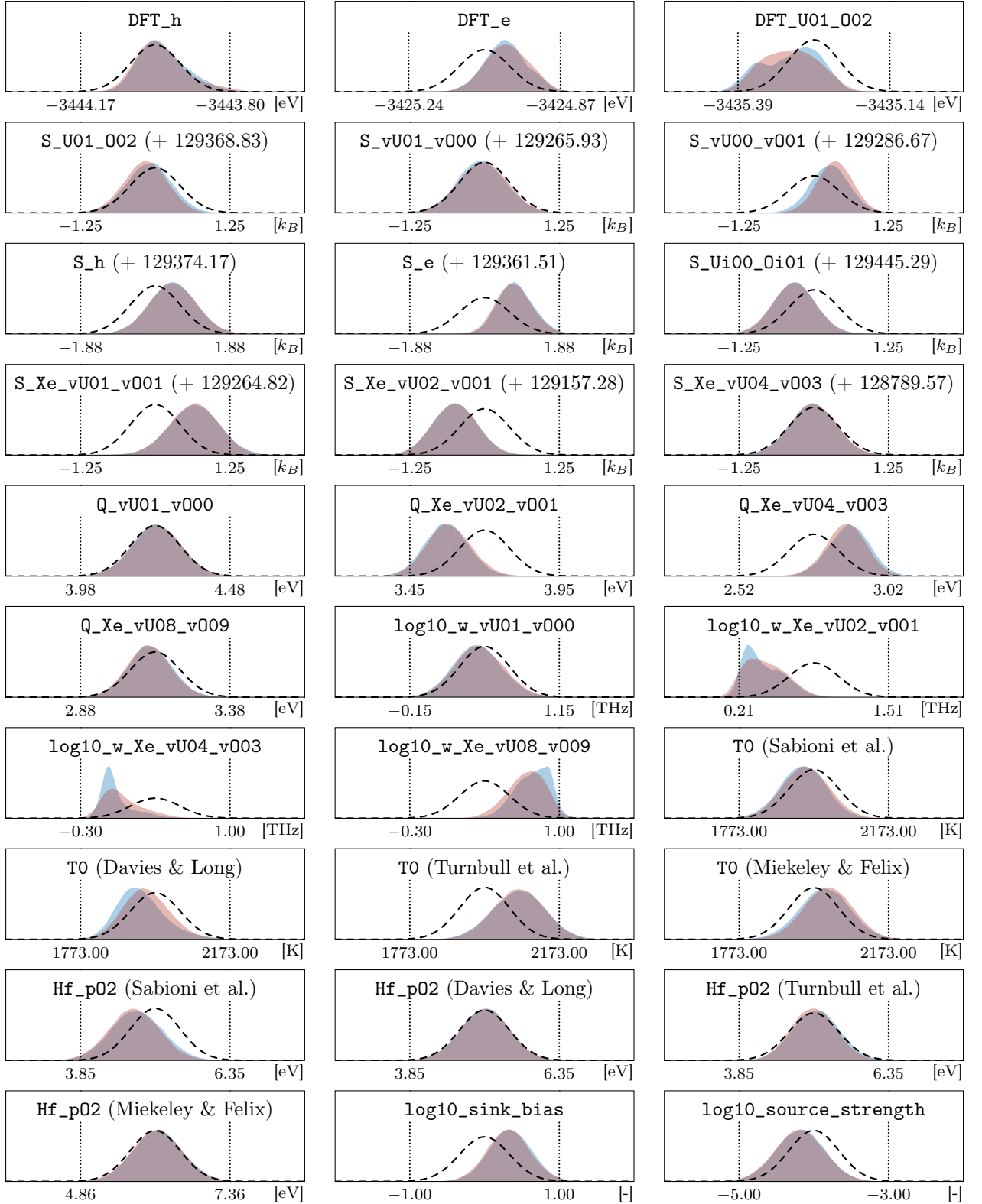


Figure 12: Probability density function of the prior (---), marginal posterior (■) and marginal posterior with weighted likelihood (■) for all parameters. The lower and upper bounds used to construct the PCE surrogate models are indicated by the vertical lines (.....). A number next to a parameter name indicates that the corresponding value needs to be added to the shown parameter bounds. Note that the DFT parameters represent total energies from DFT calculations as used by *Centipede*, and that entropies are presented in a reduced form suitable for *Centipede* and should not be interpreted as an actual entropy, see [5, 17, 58].

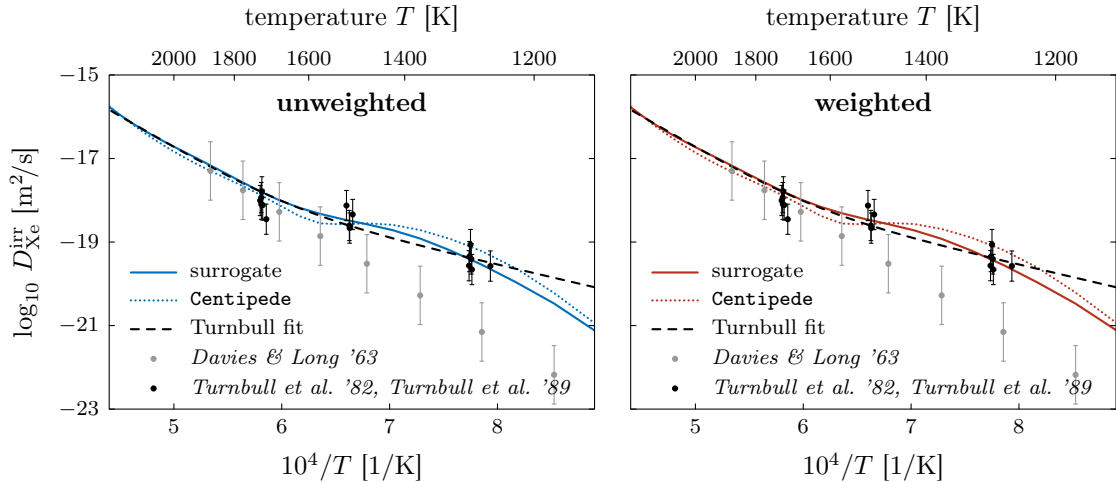


Figure 13: Pushforward MAP prediction for the xenon diffusivity under irradiation with the surrogate (*solid line*) and pushforward MAP prediction of **Centipede** (*dotted line*) for both the unweighted likelihood (*left*) and the weighted likelihood from [equation \(7\)](#). Also shown are the Turnbull et al. measurements for the diffusivity under irradiation from [\[7, 9\]](#) and the Davies & Long measurements for the intrinsic diffusivity from [\[5\]](#), together with the fit by Turnbull et al. (*dashed line*). Note the excellent agreement between the predicted xenon diffusivity and the Turnbull et al. fit from the data for high temperatures.

## 6 Conclusion and further work

The fission gas diffusivity coefficient is one of the crucial parameters used in many nuclear fuel performance models. Reconciling existing models, such as the cluster dynamics simulation software **Centipede**, with historical gas release and thermodynamic data is crucial to predict the behavior of fission gas for both current and novel nuclear fuel types. In this work, we have developed a Bayesian calibration framework for **Centipede**. Our approach provides a posterior distribution on the atomistic parameters in the model underlying the cluster dynamics simulator. A particular challenge in our setup is that only summary statistics (i.e., a measurement value with an associated uncertainty) of the experiments have been reported in the literature. We have employed a DFI approach that uses synthetic data sets in order to match the pushforward predictions of the uranium and xenon diffusivity, as well as the non-stoichiometry of  $\text{UO}_{2\pm x}$ , with the available summary statistics. In a departure from the original DFI framework, our construction uses a stochastic optimization argument to enforce consistency of the statistics computed from the pushforward posterior and the reported summary statistics. Further, we reduce computational costs significantly by replacing the expensive evaluations of **Centipede** with evaluations from a reduced PCE surrogate model. This reduced model was identified using a sensitivity analysis. We also constructed a weighted variant of our method, where we compensate for the number of measurements in each set of experimental data summaries. We found that, in both the unweighted and the weighted case, there is a good agreement between the calibrated atomistic model and the reported summary statistics. Furthermore, our results are in good agreement with the Turnbull et al. fit for the xenon diffusivity reported in [\[9\]](#). The latter analysis has been used as a starting point for many higher-level fission gas release models, as it sets the timescale for the subsequent percolation of gas bubbles at grain boundaries. The excellent agreement between the estimated xenon diffusivity from calibration and the empirical fits based on experimental data confirms that a uranium vacancy-based mechanism can describe the xenon diffusion under irradiation conditions predicted from the experimental data.

**Centipede** is part of a larger, hierarchical multiscale modelling and simulation framework used to simulate the complete fission gas release process, see, e.g. [\[2\]](#). Uncertainty quantification (UQ) has a critical role to play in connecting these different models at different length and time scales. While

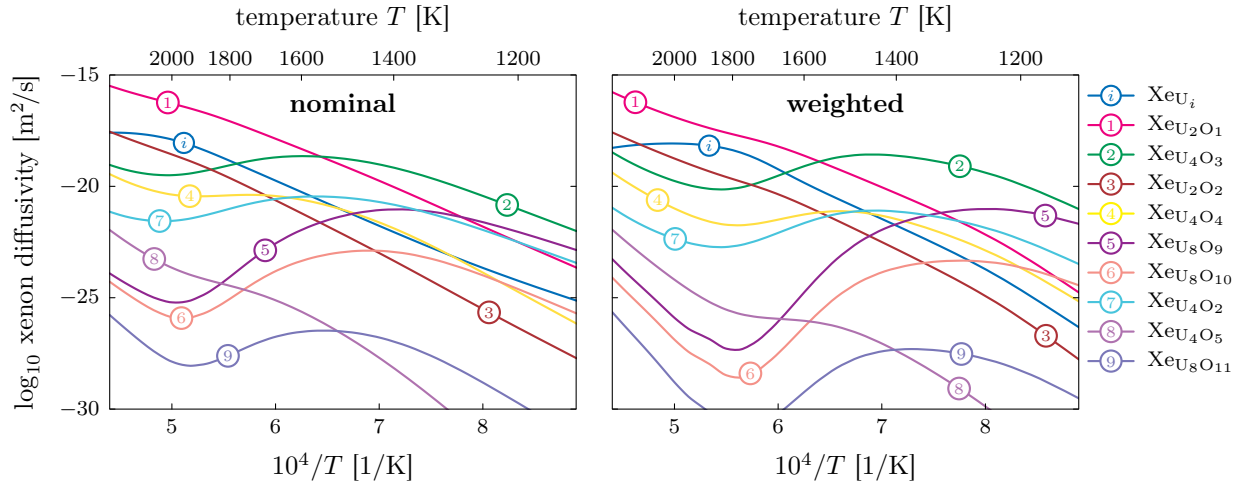


Figure 14: Contributions of the individual defects to the xenon diffusivity under irradiation, for the 10 most important defects, for both the nominal parameter values (*left*) and the estimated parameters using the weighted likelihood formulation (*right*).

our current work provides a demonstration of the application of UQ by calibrating atomistic-scale parameters in one of the lower-level mechanistic models for fission gas release, the same calibration strategy can be used for higher-level codes in the framework, such as `Xolotl-MARMOT`, see [37, 59], `BISON` [60, 61] and `Nyx` [62, 63].

In future work, we will use our calibration strategy to predict the fission gas evolution at the fuel pin scale, simulated by the fuel performance code `Nyx`, see [59], and using experimental data from, amongst others, [64]. The fuel performance code will also use the calibrated xenon diffusivity as input. The simulations performed by `Nyx` may easily be transferred to a full-fledged fuel performance code such as `BISON` afterwards. The xenon diffusivity can also be used to determine the impact of fission gas evolution at the grain scale using coupled `Xolotl-MARMOT`.

## Acknowledgements

This work was supported by the U.S. Department of Energy, Office of Nuclear Energy and Office of Science, Office of Advanced Scientific Computing Research through the Scientific Discovery through Advanced Computing project on Simulation of Fission Gas.

This research made use of the resources of the High Performance Computing Center at Idaho National Laboratory, which is supported by the Office of Nuclear Energy of the U.S. Department of Energy and the Nuclear Science User Facilities under Contract No. DE-AC07-05ID14517.

This article has been co-authored by employees of National Technology & Engineering Solutions of Sandia, LLC under Contract No. DE-NA0003525 with the U.S. Department of Energy (DOE). The employees co-own right, title and interest in and to the article and are responsible for its contents. The United States Government retains and the publisher, by accepting the article for publication, acknowledges that the United States Government retains a non-exclusive, paid-up, irrevocable, world-wide license to publish or reproduce the published form of this article or allow others to do so, for United States Government purposes. The DOE will provide public access to these results of federally sponsored research in accordance with the DOE Public Access Plan <https://www.energy.gov/downloads/doe-public-access-plan>.

Los Alamos National Laboratory, an affirmative action/equal opportunity employer, is operated by Triad National Security, LLC, for the National Nuclear Security Administration of the U.S. Department of Energy under Contract No. 89233218CNA000001.

## References

- [1] D Olander. Nuclear fuels—present and future. *J. Nucl. Mater.*, 389(1):1–22, 2009.
- [2] D.A. Andersson, P. Garcia, X.-Y. Liu, G. Pastore, M. Tonks, P. Millett, B. Dorado, D.R. Gaston, D. Andrs, R.L. Williamson, R.C. Martineau, B.P. Uberuaga, and C.R. Stanek. Atomistic modeling of intrinsic and radiation-enhanced fission gas (Xe) diffusion in  $\text{UO}_{2\pm x}$ : Implications for nuclear fuel performance modeling. *J. Nucl. Mater.*, 451:225–242, 2014.
- [3] David A Andersson, Michael R Tonks, Luis Casillas, Shyam Vyas, Pankaj Nerikar, Blas P Uberuaga, and Christopher R Stanek. Multiscale simulation of xenon diffusion and grain boundary segregation in  $\text{UO}_2$ . *J. Nucl. Mater.*, 462:15–25, 2015.
- [4] Thomas Cardinaels, Kevin Govers, Benedict Vos, Sven Van den Berghe, Marc Verwerft, L De Tollenaere, G Maier, and C Delafoy. Chromia doped  $\text{UO}_2$  fuel: Investigation of the lattice parameter. *J. Nucl. Mater.*, 424(1-3):252–260, 2012.
- [5] D Davies and G Long. The emission of Xe-133 from lightly irradiated uranium dioxide spheroids and powders. Technical Report AERE 4347, Atomic Energy Research Establishment, Harwell, 1963.
- [6] Hj Matzke. Gas release mechanisms in  $\text{UO}_2$  – a critical review. *Radiat. Eff.*, 53(3-4):219–242, 1980.
- [7] JA Turnbull, RJ White, and C Wise. The diffusion coefficient for fission gas atoms in uranium dioxide. Technical report, International Atomic Energy Agency (IAEA), Vienna (Austria), 1989.
- [8] Romain Perriot, Christopher Matthews, Michael W.D. Cooper, Blas P. Uberuaga, Christopher R. Stanek, and David A. Andersson. Atomistic modeling of out-of-pile xenon diffusion by vacancy clusters in  $\text{UO}_2$ . *J. Nucl. Mater.*, 520:96–109, 2019.
- [9] JA Turnbull, CA Friskney, JR Findlay, FA Johnson, and AJ Walter. The diffusion coefficients of gaseous and volatile species during the irradiation of uranium dioxide. *J. Nucl. Mater.*, 107:168–184, 1982.
- [10] J Rest, MWD Cooper, J Spino, JA Turnbull, P Van Uffelen, and CT Walker. Fission gas release from  $\text{UO}_2$  nuclear fuel: A review. *J. Nucl. Mater.*, 513:310–345, 2019.
- [11] Charles Richard Arthur Catlow. Fission gas diffusion in uranium dioxide. *Proc. R. Soc. A: Math. Phys. Eng. Sci.*, 364(1719):473–497, 1978.
- [12] RA Jackson, AD Murray, JH Harding, and CRA Catlow. The calculation of defect parameters in  $\text{UO}_2$ . *Philos. Mag.*, 53(1):27–50, 1986.
- [13] RW Grimes and Charles Richard Arthur Catlow. The stability of fission products in uranium dioxide. *Philos. Trans., Math. Phys. Eng. Sci.*, 335(1639):609–634, 1991.
- [14] Younsuk Yun, Hanchul Kim, Heemoon Kim, and Kwangheon Park. Atomic diffusion mechanism of Xe in  $\text{UO}_2$ . *J. Nucl. Mater.*, 378(1):40–44, 2008.
- [15] Kevin Govers, SE Lemehov, and Marc Verwerft. On the solution and migration of single Xe atoms in uranium dioxide – An interatomic potentials study. *J. Nucl. Mater.*, 405(3):252–260, 2010.
- [16] Emily Moore, Christine Guéneau, and Jean-Paul Crocombette. Diffusion model of the non-stoichiometric uranium dioxide. *J. Solid State Chem.*, 203:145–153, 2013.

- [17] Michael William D Cooper, Christopher Richard Stanek, James Anthony Turnbull, Blas P Uberuaga, and David Anders Andersson. Simulation of radiation driven fission gas diffusion in  $\text{UO}_2$ ,  $\text{ThO}_2$  and  $\text{PuO}_2$ . *J. Nucl. Mater.*, 481:125–133, 2016.
- [18] Christopher Matthews, Romain Perriot, Michael W.D. Cooper, Christopher R. Stanek, and David A. Andersson. Cluster dynamics simulation of uranium self-diffusion during irradiation in  $\text{UO}_2$ . *J. Nucl. Mater.*, 527:151787, 2019.
- [19] Christopher Matthews, Romain Perriot, M.W.D Cooper, Christopher R. Stanek, and David A. Andersson. Cluster dynamics simulation of xenon diffusion during irradiation in  $\text{UO}_2$ . *J. Nucl. Mater.*, 540:152326, 2020.
- [20] TL Markin, VJ Wheeler, and RJ Bones. High temperature thermodynamic data for  $\text{UO}_{2\pm x}$ . *J. Inorg. Nucl. Chem.*, 30(3):807–817, 1968.
- [21] VJ Wheeler. High temperature thermodynamic data for  $\text{UO}_{2\pm x}$ . *J. Nucl. Mater.*, 39(3):315–318, 1971.
- [22] VJ Wheeler and IG Jones. Thermodynamic and composition changes in  $\text{UO}_{2\pm x}$  ( $x < 0.005$ ) at 1950K. *J. Nucl. Mater.*, 42(2):117–121, 1972.
- [23] NA Javed. Thermodynamic study of hypostoichiometric urania. *J. Nucl. Mater.*, 43(3):219–224, 1972.
- [24] S t Aronson and J Belle. Nonstoichiometry in uranium dioxide. *J. Chem. Phys.*, 29(1):151–158, 1958.
- [25] K Une and M Oguma. Oxygen potentials of (U, Gd)  $\text{O}_{2\pm x}$  solid solutions in the temperature range 1000–1500°C. *J. Nucl. Mater.*, 115(1):84–90, 1983.
- [26] K Une and M Oguma. Thermodynamic properties of nonstoichiometric urania-gadolinia solid solutions in the temperature range 700–1100°C. *J. Nucl. Mater.*, 110(2-3):215–222, 1982.
- [27] Kjell Hagemark and M Broli. Equilibrium oxygen pressures over the nonstoichiometric uranium oxides  $\text{UO}_{2+x}$  and  $\text{U}_3\text{O}_{8-z}$  at higher temperatures. *J. Inorg. Nucl. Chem.*, 28(12):2837–2850, 1966.
- [28] Antonio Claret Soares Sabioni, Wilmar Barbosa Ferraz, and F Millot. First study of uranium self-diffusion in  $\text{UO}_2$  by sims. *J. Nucl. Mater.*, 257:180–184, 1998.
- [29] Robert D Berry, Habib N Najm, Bert J Debusschere, Youssef M Marzouk, and Helgi Adalsteins-son. Data-free inference of the joint distribution of uncertain model parameters. *J. Comput. Phys.*, 231(5):2180–2198, 2012.
- [30] Habib N Najm, Robert D Berry, Cosmin Safta, Khachik Sargsyan, and Bert J Debusschere. Data-free inference of uncertain parameters in chemical models. *Int. J. Uncertain. Quantif.*, 4(2), 2014.
- [31] Kenny Chowdhary and Habib N Najm. Data free inference with processed data products. *Stat. Comput.*, 26(1):149–169, 2016.
- [32] Mohammad Khalil, Kenny Chowdhary, Cosmin Safta, Khachik Sargsyan, and Habib N Najm. Inference of reaction rate parameters based on summary statistics from experiments. *Proc. Combust. Inst.*, 36(1):699–708, 2017.
- [33] Tiernan A Casey and Habib N Najm. Estimating the joint distribution of rate parameters across multiple reactions in the absence of experimental data. *Proc. Combust. Inst.*, 37(1):797–805, 2019.

- [34] R.G. Ghanem and P.D. Spanos. *Stochastic Finite Elements: A Spectral Approach*. Springer Verlag, New York, 1991.
- [35] H.N. Najm. Uncertainty quantification and polynomial chaos techniques in computational fluid dynamics. *Annu. Rev. Fluid Mech.*, 41(1):35–52, 2009.
- [36] W Miekeley and FW Felix. Effect of stoichiometry on diffusion of xenon in UO<sub>2</sub>. *J. Nucl. Mater.*, 42(3):297–306, 1972.
- [37] David Bernholdt, James Kress, Alexander McCaskey, Philip Roth, Philip Fackler, Sophie Blondel, Crystal Jernigan, Dwaipayana Dasgupta, Danqing We, Christopher Ulmer, Gerrit VanCoevering, Sam Morris, Barry Smith, Habib Najm, Ozgur Cekmer, Dong-Uk Kim, Jay Billings, Omar Knio, and Brian Wirth. *Xo1ot1*. DOE CODE, Department of Energy (DOE), Office of Scientific and Technical Information (OSTI), <https://www.osti.gov/doi/10.2172/1809000>, 2022.
- [38] Steve Brooks, Andrew Gelman, Galin Jones, and Xiao-Li Meng. *Handbook of Markov chain Monte Carlo*. CRC press, 2011.
- [39] Edwin T Jaynes. Information theory and statistical mechanics. *Phys. Rev.*, 106(4):620–630, 1957.
- [40] Edwin T Jaynes. Information theory and statistical mechanics II. *Phys. Rev.*, 108(2):171–190, 1957.
- [41] Christian Genest, Kevin J McConway, and Mark J Schervish. Characterization of externally Bayesian pooling operators. *Ann. Stat.*, pages 487–501, 1986.
- [42] James C Spall. Stochastic optimization. In *Handbook of computational statistics*, pages 173–201. Springer, 2012.
- [43] R. Ghanem. Ingredients for a general purpose stochastic finite element formulation. *Comput. Methods. Appl. Mech. Eng.*, 168:19–34, 1999.
- [44] Olivier Le Maître, Omar M Knio, Habib N Najm, and Roger G Ghanem. A stochastic projection method for fluid flow: I. Basic formulation. *J. Comput. Phys.*, 173(2):481–511, 2001.
- [45] Matthew T Reagan, Habib N Najm, Roger G Ghanem, and Omar M Knio. Uncertainty quantification in reacting-flow simulations through non-intrusive spectral projection. *Combust. Flame.*, 132(3):545–555, 2003.
- [46] Oliver G Ernst, Antje Mugler, Hans-Jörg Starkloff, and Elisabeth Ullmann. On the convergence of generalized polynomial chaos expansions. *ESAIM: Math. Model. Numer. Anal.*, 46(2):317–339, 2012.
- [47] Khachik Sargsyan. Surrogate models for uncertainty propagation and sensitivity analysis. In Roger Ghanem, D Higdon, and H Owhadi, editors, *Handbook of uncertainty quantification*, pages 1–26. Springer, Cham, Switzerland, 2017.
- [48] B.J. Debusschere, H.N. Najm, P.P. Pébay, O.M. Knio, R.G. Ghanem, and O.P. Le Maître. Numerical challenges in the use of polynomial chaos representations for stochastic processes. *SIAM J. Sci. Comput.*, 26:698–719, 2004.
- [49] Khachik Sargsyan, Cosmin Safta, Habib N Najm, Bert J Debusschere, Daniel Ricciuto, and Peter Thornton. Dimensionality reduction for complex models via Bayesian compressive sensing. *Int. J. Uncertain. Quantif.*, 4(1), 2014.

- [50] Ilya M Sobol. Global sensitivity indices for nonlinear mathematical models and their Monte Carlo estimates. *Math. Comput. Simulat.*, 55(1-3):271–280, 2001.
- [51] Thierry Crestaux, Olivier Le Maître, and Jean-Marc Martinez. Polynomial chaos expansion for sensitivity analysis. *Reliab. Eng. Syst.*, 94(7):1161–1172, 2009.
- [52] Andrea Saltelli, Marco Ratto, Terry Andres, Francesca Campolongo, Jessica Cariboni, Debora Gatelli, Michaela Saisana, and Stefano Tarantola. *Global sensitivity analysis: the primer*. John Wiley & Sons, 2008.
- [53] Cody J Permann, Derek R Gaston, David Andrš, Robert W Carlsen, Fande Kong, Alexander D Lindsay, Jason M Miller, John W Peterson, Andrew E Slaughter, Roy H Stogner, et al. Moose: Enabling massively parallel multiphysics simulation. *SoftwareX*, 11:100430, 2020.
- [54] Benjamin S Kirk, John W Peterson, Roy H Stogner, and Graham F Carey. libmesh: a C++ library for parallel adaptive mesh refinement/coarsening simulations. *Eng. Comput.*, 22(3):237–254, 2006.
- [55] Satish Balay, Shrirang Abhyankar, Mark F. Adams, Steven Benson, Jed Brown, Peter Brune, Kris Buschelman, Emil M. Constantinescu, Lisandro Dalcin, Alp Dener, Victor Eijkhout, William D. Gropp, Václav Hapla, Tobin Isaac, Pierre Jolivet, Dmitry Karpeev, Dinesh Kaushik, Matthew G. Knepley, Fande Kong, Scott Kruger, Dave A. May, Lois Curfman McInnes, Richard Tran Mills, Lawrence Mitchell, Todd Munson, Jose E. Roman, Karl Rupp, Patrick Sanan, Jason Sarich, Barry F. Smith, Stefano Zampini, Hong Zhang, Hong Zhang, and Junchao Zhang. PETSc Web page, 2022.
- [56] B. Debuschere, K. Sargsyan, C. Safta, and K. Chowdhary. The uncertainty quantification toolkit (UQTK). In R. Ghanem, D. Higdon, and H. Owhadi, editors, *Handbook of Uncertainty Quantification*, pages 1807–1827. Springer, 2017.
- [57] Dong C Liu and Jorge Nocedal. On the limited memory BFGS method for large scale optimization. *Math. Program. Comput.*, 45(1):503–528, 1989.
- [58] X-Y Liu, Christopher Matthews, Wen Jiang, Michael William Donald Cooper, JD Hales, and DA Andersson. Atomistic and cluster dynamics modeling of fission gas (Xe) diffusivity in TRISO fuel kernels. *J. Nucl. Mater.*, 561:153539, 2022.
- [59] Dong-Uk Kim, Sophie Blondel, David E Bernholdt, Philip Roth, Fande Kong, David Andersson, Michael R Tonks, and Brian D Wirth. Modeling mesoscale fission gas behavior in UO<sub>2</sub> by directly coupling the phase field method to spatially resolved cluster dynamics. *Mater. Theory*, 6(1):1–28, 2022.
- [60] Richard L Williamson, JD Hales, SR Novascone, MR Tonks, DR Gaston, CJ Permann, D Anders, and RC Martineau. Multidimensional multiphysics simulation of nuclear fuel behavior. *J. Nucl. Mater.*, 423(1-3):149–163, 2012.
- [61] Richard L Williamson, Jason D Hales, Stephen R Novascone, Giovanni Pastore, Kyle A Gamble, Benjamin W Spencer, Wen Jiang, Stephanie A Pitts, Albert Casagrande, Daniel Schwen, et al. BISON: A flexible code for advanced simulation of the performance of multiple nuclear fuel forms. *Nucl. Technol.*, 207(7):954–980, 2021.
- [62] D. Pizzocri, G. Pastore, T. Barani, A. Magni, L. Luzzi, P. Van Uffelen, S.A. Pitts, A. Alfonsi, and J.D. Hales. A model describing intra-granular fission gas behaviour in oxide fuel for advanced engineering tools. *J. Nucl. Mater.*, 502:323–330, 2018.
- [63] G. Pastore, N. Militello, D. Blondel, and B. D. Wirth. Single-size and cluster dynamics modeling of intra-granular fission gas bubbles in UO<sub>2</sub>. *J. Nucl. Mater.*, 2022. Submitted.

- [64] C Baker. The fission gas bubble distribution in uranium dioxide from high temperature irradiated SGHWR fuel pins. *J. Nucl. Mater.*, 66:283–291, 1977.
- [65] Nicholas Metropolis, Arianna W Rosenbluth, Marshall N Rosenbluth, Augusta H Teller, and Edward Teller. Equation of state calculations by fast computing machines. *J. Chem. Phys.*, 21(6):1087–1092, 1953.
- [66] Heikki Haario, Eero Saksman, and Johanna Tamminen. An adaptive Metropolis algorithm. *Bernoulli*, pages 223–242, 2001.
- [67] Yves F Atchadé and Jeffrey S Rosenthal. On adaptive Markov chain Monte Carlo algorithms. *Bernoulli*, 11(5):815–828, 2005.

## Appendix A Supplementary data

The temperatures where **Centipede** predicts the diffusivities  $D_U^{\text{theq}}$ ,  $D_{\text{Xe}}^{\text{theq}}$  and  $D_{\text{Xe}}^{\text{irr}}$  are included in [Table 3](#). The available experimental data summaries are shown in [Tables 4 to 8](#), where  $\mathbf{x}_d^{(n)}$ ,  $y_d^{(n)}$  and  $s_d^{(n)}$  are as defined in [equation \(3\)](#). The nominal values, lower and upper bounds for each parameter are shown in [Table 9](#). Estimated parameter values obtained after calibration are compiled in [Table 10](#).

#	$T$ [K]	#	$T$ [K]	#	$T$ [K]	#	$T$ [K]
1	1123	8	1473	15	1823	22	2073
2	1173	9	1523	16	1873	23	2123
3	1223	10	1573	17	1923	24	2173
4	1273	11	1623	18	1948	25	2223
5	1323	12	1673	19	1973	26	2273
6	1373	13	1723	20	1998		
7	1423	14	1773	21	2023		

Table 3: Temperatures  $T$  [K] where the **Centipede** predictions of  $D_U^{\text{theq}}$ ,  $D_{\text{Xe}}^{\text{theq}}$  and  $D_{\text{Xe}}^{\text{irr}}$  are available.

$n$	$\mathbf{x}_1^{(n)}$ $T$ [K]	$y_1^{(n)}$ $D_U^{\text{theq}}$ [m <sup>2</sup> /s]	$s_1^{(n)}$ $\pm$ [m <sup>2</sup> /s]
1	1971.434	-21.277	0.166
2	1963.456	-21.320	0.166
3	1972.562	-21.503	0.166
4	1920.864	-21.738	0.166
5	1870.564	-21.951	0.166
6	1871.075	-22.292	0.166
7	1820.237	-22.100	0.166
8	1820.237	-22.535	0.166
9	1770.560	-22.538	0.166
10	1769.811	-22.735	0.166

Table 4: Sabioni et al. data set ( $d = 1$ ) from [\[28\]](#).

$n$	$\mathbf{x}_2^{(n)}$ $T$ [K]	$y_2^{(n)}$ $D_{\text{Xe}}^{\text{theq}}$ [m <sup>2</sup> /s]	$s_2^{(n)}$ $\pm$ [m <sup>2</sup> /s]
1	1173.000	-22.179	0.699
2	1273.000	-21.153	0.699
3	1373.000	-20.277	0.699
4	1473.000	-19.519	0.699
5	1573.000	-18.858	0.699
6	1673.000	-18.276	0.699
7	1773.000	-17.760	0.699
8	1873.000	-17.298	0.699

Table 5: Davies & Long data set ( $d = 2$ ) from [\[5\]](#).

$n$	$\mathbf{x}_3^{(n)}$ $T$ [K]	$y_3^{(n)}$ $D_{\text{Xe}}^{\text{irr}}$ [m <sup>2</sup> /s]	$s_3^{(n)}$ $\pm$ [m <sup>2</sup> /s]
1	1724.138	-18.006	0.362
2	1721.170	-17.935	0.362
3	1720.994	-18.093	0.362
4	1719.484	-17.798	0.362
5	1717.193	-18.114	0.362
6	1707.520	-18.453	0.362
7	1515.152	-18.126	0.362
8	1509.013	-18.604	0.362
9	1508.296	-18.666	0.362
10	1502.045	-18.340	0.362
11	1292.608	-19.565	0.362
12	1291.990	-19.348	0.362
13	1290.323	-19.060	0.362
14	1289.010	-19.405	0.362
15	1288.215	-19.658	0.362
16	1260.345	-19.575	0.362

Table 6: Turnbull et al. data set ( $d = 3$ ) from [7, 9].

$n$	$\mathbf{x}_4^{(n)}$ $T$ [K]	$y_4^{(n)}$ $D_{Xe}^{\text{theq}}$ [m <sup>2</sup> /s]	$s_4^{(n)}$ $\pm$ [m <sup>2</sup> /s]
1	1967.849	-14.220	2.094
2	1929.348	-14.254	2.280
3	1974.416	-14.608	1.669
4	1892.324	-14.946	1.807
5	1800.203	-14.963	2.376
6	1822.382	-15.014	2.179
7	1794.742	-15.082	2.294
8	1773.227	-15.606	1.917
9	1731.707	-15.656	2.159
10	1706.731	-15.707	2.291
11	1736.791	-15.758	2.021
12	1816.786	-15.961	1.269
13	1696.941	-15.301	2.770
14	1626.948	-15.927	2.694
15	1701.822	-16.113	1.922
16	1600.541	-16.130	2.711
17	1618.049	-16.265	2.430
18	1631.434	-16.552	2.032
19	1649.628	-16.569	1.869
20	1731.707	-16.434	1.381
21	1518.392	-16.806	2.768
22	1550.218	-17.296	1.985
23	1583.408	-17.262	1.725
24	1645.042	-17.414	1.061
25	1484.114	-17.685	2.219
26	1465.731	-17.786	2.300
27	1440.747	-17.735	2.607
28	1491.597	-17.887	1.942
29	1506.791	-18.361	1.323
30	1361.196	-18.614	2.608
31	1426.849	-19.003	1.486
32	1223.294	-20.254	2.763

Table 7: Miekeley & Felix data set ( $d = 4$ ) from [36].

$n$	$T$ [K]	$\mathbf{x}_5^{(n)}$	$y_5^{(n)}$	$s_5^{(n)}$	$n$	$T$ [K]	$\mathbf{x}_5^{(n)}$	$y_5^{(n)}$	$s_5^{(n)}$
		$\log_{10}(p_{\text{O}_2})$ [atm]	$\text{UO}_{2\pm x}$ ( $\times 1,000$ )	$\pm$ ( $\times 1,000$ )			$\log_{10}(p_{\text{O}_2})$ [atm]	$\text{UO}_{2\pm x}$ ( $\times 1,000$ )	$\pm$ ( $\times 1,000$ )
1	1800	-18.043	0.000	1.000	53	1043	-18.740	0.558	0.252
2	1800	-18.359	-1.000	1.000	54	1043	-18.745	0.801	0.252
3	1800	-18.638	-2.000	1.000	55	1043	-18.660	1.000	0.252
4	1800	-18.979	-3.000	1.000	56	1043	-18.444	1.000	0.252
5	1900	-16.288	0.000	1.000	57	1043	-18.200	1.000	0.252
6	1900	-16.656	-3.000	1.000	58	1043	-18.270	0.812	0.252
7	1900	-16.910	-2.000	1.000	59	1043	-18.080	0.799	0.252
8	2000	-15.386	-3.000	1.000	60	1043	-17.719	0.805	0.252
9	1950	-16.498	-1.800	0.300	61	1043	-17.526	1.000	0.252
10	1950	-15.893	-0.900	0.300	62	1043	-17.000	1.000	0.252
11	1950	-15.411	-0.400	0.300	63	1043	-17.772	2.000	0.252
12	1950	-14.593	0.000	0.300	64	1043	-17.323	2.000	0.252
13	1950	-9.717	0.400	0.300	65	1043	-16.593	2.000	0.252
14	1950	-8.967	1.200	0.300	66	1043	-15.889	1.000	0.252
15	1950	-8.519	2.100	0.300	67	1043	-15.441	2.000	0.252
16	1950	-7.924	2.500	0.300	68	1043	-15.963	2.000	0.252
17	1900	-13.815	0.000	3.000	69	1043	-16.572	2.000	0.252
18	1900	-14.401	0.000	3.000	70	1043	-15.235	3.000	0.252
19	1900	-15.987	-2.000	3.000	71	1043	-14.719	3.000	0.252
20	1800	-16.391	0.000	3.000	72	1043	-14.255	3.000	0.252
21	1800	-16.638	0.000	3.000	73	1373	-17.000	0.107	0.252
22	1800	-17.666	-2.000	3.000	74	1373	-16.013	0.294	0.252
23	1700	-18.775	0.000	3.000	75	1373	-15.249	0.603	0.252
24	1700	-19.928	0.000	3.000	76	1373	-15.330	0.891	0.252
25	1700	-20.572	-3.000	3.000	77	1373	-14.484	0.811	0.252
26	1600	-22.197	0.000	3.000	78	1373	-14.289	1.000	0.252
27	1600	-22.470	0.000	3.000	79	1373	-15.025	1.000	0.252
28	1600	-22.812	0.000	3.000	80	1373	-14.155	2.000	0.252
29	1600	-22.955	-1.000	3.000	81	1373	-13.429	2.000	0.252
30	1600	-22.824	-3.000	3.000	82	1373	-13.186	2.000	0.252
31	1273	-15.438	0.807	1.000	83	1373	-12.526	2.000	0.252
32	1273	-12.623	1.845	1.000	84	1373	-12.821	2.000	0.252
33	1573	-12.845	1.007	1.000	85	1373	-12.939	3.000	0.252
34	1573	-11.179	2.999	1.000	86	1373	-12.113	3.000	0.252
35	1773	-10.648	2.153	1.000	87	1373	-11.398	3.000	0.252
36	1273	-14.419	1.019	2.520	88	1373	-10.967	3.000	0.252
37	1273	-13.054	1.879	2.520	89	1373	-10.654	3.000	0.252
38	1172.791	-12.112	2.000	0.700	90	1473	-12.921	0.715	0.252
39	1272.316	-11.195	2.000	0.700	91	1473	-11.947	1.000	0.252
40	1371.829	-10.343	2.000	0.700	92	1473	-10.232	2.000	0.252
41	1472.321	-9.971	2.000	0.700	93	1473	-9.764	2.000	0.252
42	1572.005	-9.442	2.000	0.700	94	1473	-9.583	3.000	0.252
43	1672.690	-8.951	2.000	0.700	95	1573	-12.745	0.869	0.252
44	1772.402	-8.456	2.000	0.700	96	1573	-10.975	2.000	0.252
45	930	-22.298	0.310	2.520	97	1573	-9.708	2.000	0.252
46	930	-21.171	0.572	2.520	98	1673	-9.848	0.717	0.252
47	930	-19.409	1.000	2.520	99	1673	-8.873	2.000	0.252
48	930	-18.077	2.000	2.520	100	1673	-8.592	3.000	0.252
49	1043	-22.266	0.087	2.520	101	1986.5	-9.646	0.386	0.252
50	1043	-20.498	0.310	2.520	102	1986.5	-8.896	1.000	0.252
51	1043	-19.836	0.551	2.520	103	1986.5	-8.456	2.000	0.252
52	1043	-19.728	0.592	2.520	104	1986.5	-7.851	2.000	0.252

Table 8: Thermodynamic data set ( $d = 5$ ) for the non-stoichiometry from [20–27].

parameter name	nominal value	DFT [eV]		nominal value	s [eV/K]	
		lower bound	upper bound		lower bound	upper bound
..._Xe_Ui01_Oi00	-3425.8334	-3425.9584	-3425.7084	-129 446.1222	-129 447.3722	-129 444.8722
..._U01_002	-3435.2645	-3435.3895	-3435.1395	-129 368.8308	-129 370.0808	-129 367.5808
..._vU01_v000	-3381.0370	-3381.1620	-3380.9120	-129 265.9303	-129 267.1803	-129 264.6803
..._vU00_v001	-3443.2509	-3443.3759	-3443.1259	-129 286.6685	-129 287.9185	-129 285.4185
..._h	-3444.0477	-3444.1727	-3443.7977	-129 374.7936	-129 376.0436	-129 372.2936
..._e	-3425.1182	-3425.2432	-3424.8682	-129 362.1380	-129 363.3880	-129 359.6380
..._vU01_v001	-3389.8559	-3389.9809	-3389.7309	-129 188.3858	-129 189.6358	-129 187.1358
..._vU01_v002	-3399.7345	-3399.8595	-3399.6095	-129 107.4343	-129 108.6843	-129 106.1843
..._vU02_v000	-3324.9130	-3325.0380	-3324.7880	-129 160.7825	-129 162.0325	-129 159.5325
..._vU02_v001	-3335.6929	-3335.8179	-3335.5679	-129 080.7605	-129 082.0105	-129 079.5105
..._vU02_v002	-3346.1976	-3346.3226	-3346.0726	-129 004.2167	-129 005.4667	-129 002.9667
..._Ui01_Oi00	-3478.4152	-3478.5402	-3478.2902	-129 462.0699	-129 463.3199	-129 460.8199
..._Ui00_Oi01	-3423.4492	-3423.5742	-3423.3242	-129 445.2888	-129 446.5388	-129 444.0388
..._Ui01_Oi02	-3456.3899	-3456.5149	-3456.2649	-129 615.3049	-129 616.5549	-129 614.0549
..._Xe_vU01_v000	-3378.0494	-3378.1744	-3377.9244	-129 345.2924	-129 346.5424	-129 344.0424
..._Xe_vU01_v001	-3388.7748	-3388.8998	-3388.6498	-129 264.8194	-129 266.0694	-129 263.5694
..._Xe_vU01_v002	-3398.1568	-3398.2818	-3398.0318	-129 186.5971	-129 187.8471	-129 185.3471
..._Xe_vU02_v000	-3322.8631	-3322.9881	-3322.7381	-129 237.4063	-129 238.6563	-129 236.1563
..._Xe_vU02_v001	-3335.2667	-3335.3917	-3335.1417	-129 157.2840	-129 158.5340	-129 156.0340
..._Xe_vU02_v002	-3346.5440	-3346.6690	-3346.4190	-129 086.9852	-129 088.2352	-129 085.7352
..._Xe_vU03_v001	-3280.7401	-3280.8651	-3280.6151	-129 052.1593	-129 053.4093	-129 050.9093
..._Xe_vU03_v002	-3292.0453	-3292.1703	-3291.9203	-128 979.4136	-128 980.6636	-128 978.1636
..._Xe_vU03_v003	-3302.3153	-3302.4403	-3302.1903	-128 901.4108	-128 902.6608	-128 900.1608
..._Xe_vU03_v004	-3312.8355	-3312.9605	-3312.7105	-128 824.5474	-128 825.7974	-128 823.2974
..._Xe_vU04_v001	-3325.8450	-3325.9700	-3325.7200	-128 933.9056	-128 935.1556	-128 932.6556
..._Xe_vU04_v002	-3237.7138	-3237.8388	-3237.5888	-128 865.7380	-128 866.9880	-128 864.4880
..._Xe_vU04_v003	-3248.1971	-3248.3221	-3248.0721	-128 789.5736	-128 790.8236	-128 788.3236
..._Xe_vU04_v004	-3258.3206	-3258.4456	-3258.1956	-128 712.2956	-128 713.5456	-128 711.0456
..._Xe_vU04_v005	-3268.5677	-3268.6927	-3268.4427	-128 634.4395	-128 635.6895	-128 633.1895
..._Xe_vU04_v006	-3278.4643	-3278.5893	-3278.3393	-128 559.0793	-128 560.3293	-128 557.8293
..._Xe_vU04_v007	-3288.4526	-3288.5776	-3288.3276	-128 483.7539	-128 485.0039	-128 482.5039
..._Xe_vU05_v004	-3201.5320	-3201.6570	-3201.4070	-128 597.6268	-128 598.8768	-128 596.3768
..._Xe_vU05_v005	-3212.0795	-3212.2045	-3211.9545	-128 525.6150	-128 526.8650	-128 524.3650
..._Xe_vU05_v006	-3224.8106	-3224.9356	-3224.6856	-128 454.0513	-128 455.3013	-128 452.8013
..._Xe_vU05_v007	-3235.4855	-3235.6105	-3235.3605	-128 380.5357	-128 381.7857	-128 379.2857
..._Xe_vU05_v008	-3244.5872	-3244.7122	-3244.4622	-128 296.7549	-128 298.0049	-128 295.5049
..._Xe_vU06_v007	-3182.5388	-3182.6638	-3182.4138	-128 272.4893	-128 273.7393	-128 271.2393
..._Xe_vU06_v008	-3194.7185	-3194.8435	-3194.5935	-128 197.0652	-128 198.3152	-128 195.8152
..._Xe_vU06_v009	-3203.3341	-3203.4591	-3203.2091	-128 118.3264	-128 119.5764	-128 117.0764
..._Xe_vU07_v008	-3140.1520	-3140.2770	-3140.0270	-128 087.2454	-128 088.4954	-128 085.9954
..._Xe_vU07_v009	-3150.4497	-3150.5747	-3150.3247	-128 012.6158	-128 013.8658	-128 011.3658
..._Xe_vU07_v010	-3160.7004	-3160.8254	-3160.5754	-127 934.7572	-127 936.0072	-127 933.5072
..._Xe_vU07_v011	-3170.6988	-3170.8238	-3170.5738	-127 856.5141	-127 857.7641	-127 855.2641
..._Xe_vU08_v008	-3085.2697	-3085.3947	-3085.1447	-127 977.1638	-127 978.4138	-127 975.9138
..._Xe_vU08_v009	-3096.5023	-3096.6273	-3096.3773	-127 901.4227	-127 902.6727	-127 900.1727
..._Xe_vU08_v010	-3107.1922	-3107.3172	-3107.0672	-127 826.9061	-127 828.1561	-127 825.6561
..._Xe_vU08_v011	-3117.1919	-3117.3169	-3117.0669	-127 751.2887	-127 752.5387	-127 750.0387
..._Xe_vU08_v012	-3127.3391	-3127.4641	-3127.2141	-127 673.5524	-127 674.8024	-127 672.3024

Table 9: Nominal values, lower and upper bounds for all parameters. Note that the DFT parameters represent total energies from DFT calculations as used by **Centipede**, and that entropies are presented in a reduced form suitable for **Centipede** and should not be interpreted as an actual entropy, see [5, 17, 58].

parameter name	nominal value	Q [eV]		nominal value	log10_w [Hz]	
		lower bound	upper bound		lower bound	upper bound
..._Xe_Ui01_Oi00	1.7000	1.4500	1.9500	0	-0.3010	1
..._vU01_v000	4.2332	3.9832	4.4832	0.1523	-0.1487	1.1523
..._vU01_v001	4.1171	3.8671	4.3671	0.1523	-0.1487	1.1523
..._vU01_v002	4.3471	4.0971	4.5971	0.1523	-0.1487	1.1523
..._vU02_v000	2.4874	2.2374	2.7374	0.6972	0.3962	1.6972
..._vU02_v001	3.2656	3.0156	3.5156	0.6972	0.3962	1.6972
..._vU02_v002	3.4383	3.1883	3.6883	0.6972	0.3962	1.6972
..._Ui01_Oi00	4.0845	3.8345	4.3345	0.7364	0.4354	1.7364
..._Ui01_Oi02	1.9748	1.7248	2.2248	0.7364	0.4354	1.7364
..._Xe_vU02_v000	2.0470	1.7970	2.2970	-0.6021	-0.9031	0.3979
..._Xe_vU02_v001	3.6957	3.4457	3.9457	0.5119	0.2109	1.5119
..._Xe_vU02_v002	4.3865	4.1365	4.6365	0.2068	-0.0942	1.2068
..._Xe_vU03_v001	4.6853	4.4353	4.9353	0	-0.3010	1
..._Xe_vU03_v002	4.9853	4.7353	5.2353	0	-0.3010	1
..._Xe_vU03_v003	5.2853	5.0353	5.5353	0	-0.3010	1
..._Xe_vU03_v004	5.3457	5.0957	5.5957	0	-0.3010	1
..._Xe_vU04_v001	3.9635	3.7135	4.2135	0	-0.3010	1
..._Xe_vU04_v002	3.4635	3.2135	3.7135	0	-0.3010	1
..._Xe_vU04_v003	2.7707	2.5207	3.0207	0	-0.3010	1
..._Xe_vU04_v004	3.0707	2.8207	3.3207	0	-0.3010	1
..._Xe_vU04_v005	4.5513	4.3013	4.8013	0	-0.3010	1
..._Xe_vU04_v006	4.8513	4.6013	5.1013	0	-0.3010	1
..._Xe_vU04_v007	5.1513	4.9013	5.4013	0	-0.3010	1
..._Xe_vU05_v004	6.7700	6.2700	7.2700	0	-0.3010	1
..._Xe_vU05_v005	7.0700	6.5700	7.5700	0	-0.3010	1
..._Xe_vU05_v006	7.3700	6.8700	7.8700	0	-0.3010	1
..._Xe_vU05_v007	7.6700	7.1700	8.1700	0	-0.3010	1
..._Xe_vU05_v008	7.9700	7.4700	8.4700	0	-0.3010	1
..._Xe_vU06_v007	9.8300	9.3300	10.3300	0	-0.3010	1
..._Xe_vU06_v008	10.1300	9.6300	10.6300	0	-0.3010	1
..._Xe_vU06_v009	10.4300	9.9300	10.9300	0	-0.3010	1
..._Xe_vU07_v008	5.8600	5.3600	6.3600	0	-0.3010	1
..._Xe_vU07_v009	6.1600	5.6600	6.6600	0	-0.3010	1
..._Xe_vU07_v010	7.3000	6.8000	7.8000	0	-0.3010	1
..._Xe_vU07_v011	7.6000	7.1000	8.1000	0	-0.3010	1
..._Xe_vU08_v008	3.1290	2.8790	3.3790	0	-0.3010	1
..._Xe_vU08_v009	3.1275	2.8775	3.3775	0	-0.3010	1
..._Xe_vU08_v010	3.4347	3.1847	3.6847	0	-0.3010	1
..._Xe_vU08_v011	3.7722	3.5222	4.0222	0	-0.3010	1
..._Xe_vU08_v012	4.1797	3.9297	4.4297	0	-0.3010	1

parameter name	nominal value	unit	lower bound	upper bound
TO (Sabioni et al.)	1973	[K]	1773	2173
TO (Davies & Long)	1973	[K]	1773	2173
TO (Turnbull et al.)	1973	[K]	1773	2173
TO (Miekeley & Felix)	1973	[K]	1773	2173
Hf_p02 (Sabioni et al.)	5.1	[eV]	3.85	6.35
Hf_p02 (Davies & Long)	5.1	[eV]	3.85	6.35
Hf_p02 (Turnbull et al.)	5.1	[eV]	3.85	6.35
Hf_p02 (Miekeley & Felix)	5.1	[eV]	3.85	6.35
charge_correction_DFT	0	[eV/e <sup>2</sup> ]	0	0.0213
charge_sq_correction_DFT	0	[eV/e <sup>2</sup> ]	0	0.0569
log10_sink_strength	-2.2321	[m <sup>-2</sup> ]	-3.2321	-1.2321
log10_sink_bias	0	[-]	-1	1
log10_source_strength	-4	[s <sup>-1</sup> ]	-5	-3

Table 9: Nominal values, lower and upper bounds for all parameters in the 183-dimensional model. (continued)

parameter name	nominal value	unit	lower bound	upper bound	MAP values	
					unweighted	weighted
DFT_h	-3444.047667	[eV]	-3444.1727	-3443.7977	-3443.9877	-3444.0090
DFT_e	-3425.118167	[eV]	-3425.2432	-3424.8682	-3425.0138	-3425.0105
DFT_U01_002	-3435.2645	[eV]	-3435.3895	-3435.1395	-3435.2646	-3435.2815
S_U01_002	-129368.8308	[eV/K]	-129370.0808	-129367.5808	-129368.9301	-129368.9920
S_vU01_v000	-129265.9303	[eV/K]	-129267.1803	-129264.6803	-129265.9812	-129265.9563
S_vU00_v001	-129286.6685	[eV/K]	-129287.9185	-129285.4185	-129286.3811	-129286.3336
S_h	-129374.7936	[eV/K]	-129376.0436	-129372.2936	-129373.7106	-129373.7283
S_e	-129362.1380	[eV/K]	-129363.3880	-129359.6380	-129360.7811	-129360.7944
S_Ui00_Oi01	-129445.2888	[eV/K]	-129446.5388	-129444.0388	-129445.5613	-129445.5858
S_Xe_vU01_v001	-129264.8194	[eV/K]	-129266.0694	-129263.5694	-129264.2927	-129264.2221
S_Xe_vU02_v001	-129157.2840	[eV/K]	-129158.5340	-129156.0340	-129157.7609	-129157.7738
S_Xe_vU04_v003	-128789.5736	[eV/K]	-128790.8236	-128788.3236	-128789.5624	-128789.5619
Q_vU01_v000	4.233170	[eV]	3.9832	4.4832	4.2385	4.2393
Q_Xe_vU02_v001	3.695676	[eV]	3.4457	3.9457	3.5774	3.5792
Q_Xe_vU04_v003	2.770721	[eV]	2.5207	3.0207	2.8886	2.8732
Q_Xe_vU08_v009	3.127457	[eV]	2.8775	3.3775	3.0944	3.0949
log10_w_vU01_v000	0.152288	[Hz]	-0.1487	1.1523	0.4609	0.4594
log10_w_Xe_vU02_v001	0.511883	[Hz]	0.2109	1.5119	0.3125	0.2628
log10_w_Xe_vU04_v003	0	[THz]	-0.301	1	-0.0867	-0.0585
log10_w_Xe_vU08_v009	0	[THz]	-0.301	1	0.7639	0.6272
T0 (Sabioni et al.)	1973	[K]	1773	2173	1946.2082	1963.7078
T0 (Davies & Long)	1973	[K]	1773	2173	1930.2581	1942.0619
T0 (Turnbull et al.)	1973	[K]	1773	2173	2095.7072	2070.1338
T0 (Miekeley & Felix)	1973	[K]	1773	2173	2007.1208	2014.2658
Hf_p02 (Sabioni et al.)	5.1	[eV]	3.85	6.35	4.7613	4.6997
Hf_p02 (Davies & Long)	5.1	[eV]	3.85	6.35	5.1277	5.1278
Hf_p02 (Turnbull et al.)	5.1	[eV]	3.85	6.35	5.1028	5.0941
Hf_p02 (Miekeley & Felix)	5.1	[eV]	4.86	7.36	6.1647	6.1371
log10_sink_bias	0	[-]	-1	1	0.2423	0.2469
log10_source_strength	-4	[s <sup>-1</sup> ]	-5	-3	-4.1927	-4.2061

Table 10: Nominal values, lower and upper bounds, and MAP values with unweighted and weighted likelihoods for all estimated parameters.

---

**Algorithm 2** MCMC procedure

---

**input:** prior  $p(\boldsymbol{\nu})$ , likelihood  $\mathcal{L}(\boldsymbol{\nu})$ , starting value  $\boldsymbol{\nu}_0$ ,  
number of samples  $M$   
**output:** a set of samples  $\{\boldsymbol{\nu}_m\}_{m=1}^M$  from the posterior  $p(\boldsymbol{\nu}|\mathcal{Z}_d)$

```
1: procedure MCMC( $p(\boldsymbol{\nu}), \mathcal{L}(\boldsymbol{\nu}), \boldsymbol{\nu}_0, M$ )
2:    $\mathbf{p}_0 \leftarrow \mathcal{L}(\boldsymbol{\nu}_0)p(\boldsymbol{\nu}_0)$  // evaluate the posterior at  $\boldsymbol{\nu}_0$ 
3:   for  $m$  from 1 to  $M$  do
4:      $\boldsymbol{\nu}_{\text{prop}} \leftarrow \boldsymbol{\nu}_{m-1} + \Delta\boldsymbol{\nu}$  // generate a new proposal
5:      $\mathbf{p}_{\text{prop}} \leftarrow \mathcal{L}(\boldsymbol{\nu}_{\text{prop}})p(\boldsymbol{\nu}_{\text{prop}})$  // evaluate the posterior at  $\boldsymbol{\nu}_{\text{prop}}$ 
6:      $\alpha \leftarrow \min(1, \mathbf{p}_{\text{prop}}/\mathbf{p}_{m-1})$  // compute the acceptance ratio
7:      $u \leftarrow \mathcal{U}(0, 1)$  // sample a uniformly distributed random number
8:     if  $u < \alpha$  then
9:        $\boldsymbol{\nu}_m \leftarrow \boldsymbol{\nu}_{\text{prop}}$  and  $\mathbf{p}_m \leftarrow \mathbf{p}_{\text{prop}}$  // accept the new proposal
10:    else
11:       $\boldsymbol{\nu}_m \leftarrow \boldsymbol{\nu}_{m-1}$  and  $\mathbf{p}_m \leftarrow \mathbf{p}_{m-1}$  // reject the new proposal
12:    end if
13:  end for
14: end procedure
```

---

## Appendix B Markov chain Monte Carlo

A procedure for MCMC sampling is shown in [Algorithm 2](#). The algorithm performs a total of  $M$  MCMC iterations. In each step, we propose a jump  $\Delta\boldsymbol{\nu}$  to explore the  $s$ -dimensional parameter space. The proposal is accepted when it passes the conventional Metropolis–Hastings acceptance test in [step 8](#), here illustrated for the special case of a symmetric proposal distribution, see [\[65\]](#). The MCMC algorithm works by generating a sequence of candidates, in such a way that the distribution of these candidates approximates the desired distribution for  $M \rightarrow \infty$ . We used the adaptive MCMC (AMCMC) method proposed in [\[66, 67\]](#). In AMCMC, the proposed parameter vector  $\boldsymbol{\nu}_{\text{prop}}$  is sampled from a multivariate Gaussian centered at the current state  $\boldsymbol{\nu}_{m-1}$  with covariance  $\text{Cov}(\boldsymbol{\nu}_0, \boldsymbol{\nu}_1, \dots, \boldsymbol{\nu}_{m-1})$ . Crucially, the covariance of the proposal distribution depends on the history of the chain. Adaptive formulae that update the estimate for the covariance matrix as more and more proposals are evaluated have been provided in [\[66\]](#).

## Appendix C Trace plots

A trace plot of the Markov chain for each of the 30 parameters using the unweighted likelihood is shown in [Figure 15](#). The chain appears to be well-mixed.



Figure 15: Trace plot of the Markov chain showing the state of each parameter as a function of the iteration number. The MAP value is indicated by the dashed line. Note that the vertical axes represent the parameter value scaled to  $[-1, 1]$ . To obtain the original parameter values, these must be rescaled to the lower and upper bounds provided in [Table 9](#).